



**STUDY OF DUST PROPERTIES AROUND  
THE WHITE DWARF WD0011-399 IN  
IRIS, AKARI AND WISE SURVEYS**



A PROJECT WORK SUBMITTED TO THE  
DEPARTMENT OF PHYSICS,  
TRI-CHANDRA MULTIPLE CAMPUS  
INSTITUTE OF SCIENCE AND TECHNOLOGY  
TRIBHUVAN UNIVERSITY  
NEPAL  
FOR THE AWARD OF  
BACHELOR OF SCIENCE (B.Sc.) IN PHYSICS

BY  
SANJAY RIJAL  
SYMBOL No.: 500371235  
T.U. REGISTRATION No.: 3-2-26-255-2016  
September 12, 2022

## RECOMMENDATION

This is to recommend that Mr. Sanjay Rijal, Symbol No.: 500371235, T.U. Registration No.: 3-2-26-255-2016, has carried out the project work entitled "**STUDY OF DUST PROPERTIES AROUND THE WHITE DWARF WD0011-399 IN IRIS, AKARI AND WISE SURVEYS**" for the requirement to the project work in Bachelor of Science (B.Sc.) degree in Physics under my supervision in the Department of Physics, Tri-Chandra Multiple Campus, for the approval to the Evaluation Committee, Institute of Science and Technology (IoST), Tribhuvan University (T.U.), Nepal.

To my knowledge, this work has not been submitted for any other degree.

He has fulfilled all the requirements laid down by the Institution of Science and Technology (IoST), Tribhuvan University, Nepal for the project work for the partial fulfillment of Bachelor of Science (B.Sc.) degree.



Asst. Prof. Madhu Sudan Paudel

Supervisor

Department of Physics,  
Tri-Chandra Multiple Campus,  
Tribhuvan University,  
Ghantaghari, Kathmandu, Nepal

Date: September 12, 2022

## DECLARATION

The Project work entitled "**STUDY OF DUST PROPERTIES AROUND THE WHITE DWARF WD0011-399 IN IRIS, AKARI AND WISE SURVEYS**", is being submitted to the Department of Physics, Tri-Chandra Multiple Campus, Institute of Science and Technology (IoST), Tribhuwan University (T.U.), Nepal for the Partial Fulfillment of the requirement to the Project work in Bachelor of Science (B. Sc) degree in Physics. This Project work is carried out by me under the supervision of Asst. Prof. Madhu Sudan Paudel in the Department of Physics, Tri-Chandra Multiple Campus, Institute of Science and Technology (IoST), Tribhuwan University (T.U.), Nepal.

This work is original and has not submitted in part or full in this or any other form to any university or institute, here or elsewhere, for the award of any degree. This written submission represents my ideas in my own words and where other's ideas or words have been included; I have inadequately cited and referenced the original sources.

  
\_\_\_\_\_  
Sanjay Rijal

Symbol No: 500371235

T.U. Registration No.: 3-2-26-255-2016

Date: ..... *September 12, 2022*

## LETTER OF FORWARD

On the recommendation of Asst. Prof. Madhu Sudan Paudel, this project work is submitted by Mr. Sanjay Rijal, Symbol No. 500371235, T.U. Registration No. 3-2-26-255-2016, entitled "STUDY OF DUST PROPERTIES AROUND THE WHITE DWARF WD0011-399 IN IRIS, AKARI AND WISE SURVEYS" is forwarded by the Department of Physics, Tri-Chandra Multiple Campus, for the approval to the Evaluation Committee, Institute of Science and Technology (IoST), Tribhuvan University (T.U.), Nepal.

He has fulfilled all the requirements laid down by the Institution of Science and Technology (IoST), Tribhuvan University (T.U.), Nepal for the project work.

  
Asst. Prof. Iswar Prasad Koirala  
Head of Department  
Department of Physics, Tri-Chandra Multiple Campus,  
Tribhuvan University,  
Ghantaghari, Kathmandu, Nepal

Date: September 12, 2022

**BOARD OF EXAMINATION AND  
CERTIFICATE OF APPROVAL**

T.C. MULTIPLE CAMPUS  
1918 A.D.  
TRI-CHANDRA MULTIPLE CAMPUS  
SWATI, KATHMANDU  
KATHMANDU

This Project work (PRO-406) entitled "STUDY OF DUST PROPERTIES AROUND THE WHITE DWARF WD0011-399 IN IRIS, AKARI AND WISE SURVEYS" by Mr. Sanjay Rijal, Symbol No. 500371235 and T.U. Registration No. 3-2-26-255-201 under the supervision of Asst. Prof. Madhu Sudan Paudel in the Department of Physics, Tri-Chandra Multiple Campus, Institute of Science and Technology (IoST), Tribhuvan University (T.U.), is hereby submitted for the partial fulfillment of the Bachelor of Science (B.Sc) degree in Physics. This report has been accepted and forwarded to the Controller of Examination, Institute of Science and Technology, Tribhuvan University, Nepal for the legal procedure.



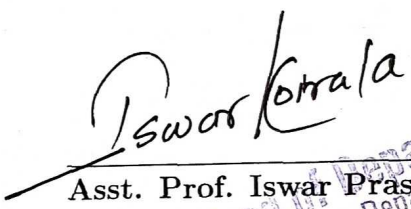
Asst. Prof. Madhu Sudan Paudel

Supervisor

Department of Physics

Tri-Chandra Multiple Campus

Ghantaghari, Kathmandu, Nepal



Asst. Prof. Iswar Prasad Koirala

Head of Department  
Physics Department  
Tri-Chandra Multiple Campus

Department of Physics

Tri-Chandra Multiple Campus

Ghantaghari, Kathmandu, Nepal



External Examiner



Internal Examiner

Date: September 12, 2022

## ACKNOWLEDGEMENTS

I would like to use this opportunity to express my deepest gratitude to my project supervisor, **Asst. Prof. Madhu Sudan Paudel**, for all the guidelines and motivation he has provided. It was an honor to have him as the project supervisor. I am very thankful to the Department of Physics, Tri-Chandra Multiple Campus for providing an opportunity to conduct this project. Specially, I wold like to convey my regards to the head of the Department of Physics, Asst. Prof. Ishwor Prasad Koirala, coordinator of the Department of Physics, Asst. Prof. Mahesh Sharma Nepal for their suggestions and encouragement.

I would also like to express my gratitude to all the professors and lecturers of B. Sc. 4th-year physics who have been a constant source of knowledge and inspiration. Namely, I would like to express my respect to Prof. Dr. Tika Bahadur Katuwal, Prof. Dr. Neelam Shrestha, Asst. Prof. Dipak Bhattarai, Asst. Prof. Gayatri Prasad Adhikari, Asst. Prof. Nar Bahadur Thami, Asst. Prof. Bhoj Raj Bhandari for helping in extending the horizon of knowledge in physics. Also, I would like to thank my classmates who have been an aid directly as well as indirectly.

Moreover, I would like to thank all the mentors of the Winter-Spring School-2021 on Scientific Computing for assisting with the programming and theoretical part which has been a massive help during the whole execution of the project. This project work is partially supported by the University Grants Commission (UGC), award no.: SRDIG-77/78-S&T-5. I would also like to express my profound appreciation to the UGC, Research Division, Sanothimi, Bhaktapur for partial funding of this project work. Last but not least, I am grateful to the SkyView Virtual Observatory, IRIS, AKARI, WISE, White Dwarf Catalog of Villanova University, SIMBAD, and Gaia Archive for the sources of data.

## ABSTRACT

This research project is focused on the study of an isolated dust structure near the white dwarf WD0011-399 located at R.A. (J2000)  $00^h 13^m 47.48^s$  and Dec. (J2000)  $-39^\circ 37' 24.28''$  using Improved Reprocessing of the IRAS (IRIS), AKARI and Wide-field Infrared Survey Explorer (WISE) surveys from SkyView Virtual Observatory along with SIMBAD Astronomical Database and Gaia Archive of ESA. The size of the cavity under study is  $5.42 \text{ pc} \times 2.75 \text{ pc}$ ,  $1.87 \text{ pc} \times 0.87 \text{ pc}$  and  $1.03 \text{ pc} \times 0.51 \text{ pc}$  with inclination angle of  $62.32^\circ$ ,  $65.57^\circ$  and  $62.27^\circ$  respectively in IRIS, AKARI and WISE data suggesting that the cavity is neither a face-on nor an edge-on. The relative flux density of the region has been studied through pixel extraction of FIR images ( $0.5^\circ$ , 30 pixels) and dust color temperature along with dust mass has been calculated. Using IRIS data the temperature of the dust structure is found between a maximum value of  $36.82 \pm 4.30 \text{ K}$  to a minimum of  $22.59 \pm 2.32 \text{ K}$  with an offset of  $14.23 \text{ K}$ . The average temperature of the region is  $28.22 \pm 0.18 \text{ K}$ . Following similar procedures for AKARI data, the temperature is found between a maximum of  $26.37 \pm 3.56 \text{ K}$  and a minimum of  $16.32 \pm 1.47 \text{ K}$  with an offset of  $10.06 \text{ K}$ . The average temperature is  $19.25 \pm 0.15 \text{ K}$ . Similarly, using WISE data, the temperature is found between a maximum of  $353.72 \pm 18.54 \text{ K}$  and a minimum of  $307.24 \pm 4.69 \text{ K}$  with an offset of  $46.48 \text{ K}$ . The average temperature is  $316.62 \pm 0.81 \text{ K}$ . The high value of offset temperature suggests that the structure might be evolving with disruptions from background radiative sources. Approximately Gaussian distribution of the temperature in all the surveys implies that the region might be tending towards local thermodynamic equilibrium. The total mass of the isolated structure is estimated to be around  $0.03 \text{ M}_\odot$ ,  $1.6 \times 10^{-3} \text{ M}_\odot$  and  $10^{-7} \text{ M}_\odot$  using IRIS, AKARI, and WISE data respectively. The Jean's mass of the structure was calculated assuming the structure a non-degenerate gas, which was estimated around  $2001.93 \text{ M}_\odot$ ,  $178.44 \text{ M}_\odot$ , and  $121.47 \text{ M}_\odot$  using IRIS, AKARI, and WISE data. Since Jean's mass is much greater than the mass of the structure there seems no possibility of star formation within the region of interest. The color maps show identical distribution for all wavelengths however, no significant relation was observed between dust color temperature and dust mass.

**Keywords:** *White Dwarf, Infrared, Dust color temperature, Dust mass, Jeans mass*

## शोधसार

यो परियोजनामा WD0011–399 नामक एक सेतो बौना ताराको समीप रहेको धुलोको संरचनाको गुणहरूको अध्ययन गरिएको छ जुन निर्देशाङ्क, दाहिने आरोहण (J2000):  $00^h 13^m 47.48^s$  र विचलन (J2000):  $-39^\circ 37' 24.28''$  मा अवस्थित छ। SkyView Virtual Observatory बाट प्राप्त भएका IRIS, AKARI र WISE खगोलिय सर्वेक्षणका FITS चित्रहरूलाई Aladin v. 9.0.0 र Python v. 3.8 मा विभिन्न माध्यमहरूबाट प्रशोधन गरि त्यस धुलोको संरचनाका गुणहरू अध्ययन तथा अवलोकन गरिएको छ। यसका साथै पिन्ड, दुरि र समीप रहेका अन्य खगोलिय वस्थुहरूको अध्ययनका लागि SIMBAD खगोलिय डाटाबेस र युरोपियन अन्तरिक्ष एजेन्सीको Gaia अभिलेखबाट आवश्यक मापदण्ड अनुसारका डाटाहरू लिइएको छ। संरचनाका अध्ययन अनुसार सो धुलोको संरचनाको आकार  $5.42 \text{ pc} \times 2.75 \text{ pc}$ ,  $1.87 \text{ pc} \times 0.87 \text{ pc}$  र  $1.03 \text{ pc} \times 0.51 \text{ pc}$  का साथै झुकाव कोण  $62.32^\circ$ ,  $65.57^\circ$  र  $62.27^\circ$  IRIS, AKARI र WISE डाटामा क्रमशः पाईएका छन्। IRIS डाटाका अनुसार सो धुलोको संरचनाको तापक्रम अधिकतम  $36.82 \pm 4.30 \text{ K}$  देखि न्युनतम  $22.59 \pm 2.32 \text{ K}$  रहनुका साथै  $14.23 \text{ K}$  को भिन्नता रहेको छ भने औसत तापक्रम  $28.22 \pm 0.18 \text{ K}$  रहेको छ। यसै गरी AKARI डाटाका अनुसार सो धुलोको संरचनाको तापक्रम अधिकतम  $26.37 \pm 3.56 \text{ K}$  देखि न्युनतम  $16.32 \pm 1.47 \text{ K}$  रहनुका साथै  $10.06 \text{ K}$  को भिन्नता रहेको छ भने औसत तापक्रम  $19.25 \pm 0.15 \text{ K}$  रहेको छ। समान प्रक्रियाहरू अपनाई WISE डाटामा सो धुलोको संरचनाको तापक्रम अधिकतम  $35.72 \pm 1.54 \text{ K}$  देखि न्युनतम  $30.7.24 \pm 4.69 \text{ K}$  रहनुका साथै  $46.48 \text{ K}$  को भिन्नता रहेको छ भने औसत तापक्रम  $31.6.62 \pm 0.81 \text{ K}$  रहेको छ। तापक्रमका भिन्नता तुलनात्मक हिसाबमा धेरै हुनुको अर्थ वरपर रहेका खगोलिय वस्तुहरूको अधिक प्रभाव रहेको भन्न सकिन्छ। साथै तापक्रमको अनुमानित Gaussian वितरण अनुसार सो संरचना ऊष्मप्रवैगिक समानतातर्फ गईरहेको भन्न सकिन्छ। संरचनाको कुल पिण्ड IRIS, AKARI र WISE डाटमा क्रमशः  $0.03$ ,  $0.0096$  र  $0.0000009$  शौर्यपिण्ड बराबर पाईएका छन्। साथै IRIS, AKARI र WISE डाटामा Jean's पिण्ड क्रमशः  $2009.93$ ,  $178.44$  र  $129.47$  शौर्यपिण्ड बराबर पाईएका छन्। सबै सर्वेक्षणहरूमा Jean's पिण्ड संरचनाको कुल पिण्ड भन्दा अत्यन्तै अधिक पाउनुको तात्पर्य सो संरचनामा नयाँ तारा बन्ने सम्भावना छैन भन्ने बुझन सकिन्छ। रंग नक्साहरूबाट सबै तरंगदैधर्य समान किसिमको आएतापनि तापक्रम र पिण्डमा भने केही सार्थक सम्बन्ध देखिएको छैन।

खोजशब्दहरू: बौना तारा, धुलोको संरचनाको तापक्रम, संरचनाको पिण्ड, Jean's पिण्ड

# LIST OF ACRONYMS AND ABBREVIATIONS

**ADQL:** Advanced Data Query Language

**AGB:** Asymptotic Giant Branch

**CDS:** Centre de données astronomiques de Strasbourg

**CSV:** Comma Separated Value

**Dec.:** Declination

**DRIBE:** Diffuse Infrared Background Experiment

**EM:** Electromagnetic

**ESA:** European Space Agency

**FIR:** Far Infrared

**FITS:** Flexible Image Transport System

**Gaia EDR3:** Gaia Early Data Release 3

**GUI:** Graphical User Interface

**Hz:** Hertz

**ICRS:** International Celestial Reference System

**IR:** Infrared

**IRAS:** Infrared Astronomical Satellite

**IRIS:** Improved Reprocessing of IRAS Survey

**ISM:** Interstellar Medium

**ISO:** Infrared Space Observatory

**ISSA:** RAS Sky Survey Atlas

**JAXA:** Japanese Aerospace Exploration Agency

**JNPS:** Journal of Nepal Physical Society

**JSON:** Java Script Object Notation

**LOS:** Line of Sight

**MSX:** Midcourse Space Experiment

**MWDD:** Montreal White Dwarf Database

**NASA:** National Aeronautics and Space Administration

**NIVR:** Netherlands Agency for Aerospace Programmes

**R.A.:** Right Ascension

**SD:** Standard Deviation

**SERC:** Science and Engineering Research Council

**SIMBAD:** Set of Identifications, Measurements and Bibliography for Astronomical Data

**TSV:** Tab Separated Value

**WD:** White Dwarf

**WISE:** Wide-field Infrared Survey Explorer

# LIST OF SYMBOLS

**H<sub>2</sub>:** Hydrogen Molecule

**μm:** Micrometer

**M<sub>⊙</sub>:** Solar Mass

**h:** Hour

**m:** Minute

**s:** Second

**°:** Degree

**':** Arc Minute

**":** Arc Second

**K:** Kelvin

**kg:** Kilogram

**J:** Joule

**T:** Temperature

**T<sub>d</sub>:** Dust Temperature

**F<sub>i</sub>:** Flux Density Emission

**λ<sub>i</sub>:** Emission Wavelength

**h:** Planck's Constant

**c:** Speed of Light in Vacuum

**k<sub>B</sub>:** Boltzmann's Constant

**N<sub>i</sub>:** Column Density of Dust Grains

**β:** Spectral Emissivity

**Ω<sub>i</sub>:** Solid Angle Subtended at Emission Wavelength

**R:** Flux Density Ratio

**B<sub>λ</sub>:** Planck's Function at wavelength  $\lambda$

**τ:** Optical Thickness

**ρ:** Grain Density

**Q<sub>λ</sub>:** Grain Emission at wavelength  $\lambda$

**D:** Distance

**G:** Universal Gravitational Constant

**P:** Pressure

**M<sub>J</sub>:** Jean's Mass

$\lambda_J$ : Jean's Length

$\mathbf{m}_H$ : Mass of Proton

$\mu$ : Average Molecular Weight of Gas

$\mathbf{q}^*$ : Intrinsic Flatness

$i$ : Inclination Angle

**v10.0**: Version 10.0

$\text{MJy sr}^{-1}$ : Mega Jansky per steradian

$\text{pc}$ : Parsec

# List of Tables

4.1	Parameters and their Values for SkyView Query Form . . . . .	22
5.1	Dimensions of Dust Structure in Different Surveys . . . . .	31
5.2	Flux Densities for Different Wavelengths . . . . .	31
5.3	Flux density Relation Between Different Wavelengths of the Same Survey . . . . .	33
5.4	Temperature Distribution for Different Wavelengths . . . . .	35
5.5	Mass of Dust, Gas and Jean's Mass for Different Surveys . . . . .	38
5.6	Inclination Angle of the Dust Structure in Different Surveys . . . . .	39
5.7	Background Sources Obtained From SIMBAD . . . . .	41

# List of Figures

1.1	Dust Clouds in ISM . . . . .	2
4.1	SkyView Query Form Interface . . . . .	15
4.2	IRAS Satellite . . . . .	16
4.3	AKARI Satellite . . . . .	17
4.4	WISE Satellite . . . . .	18
4.5	Simbad Query Interface . . . . .	19
4.6	Gaia ADQL Interface . . . . .	20
4.7	System Block Diagram (Research Plan) . . . . .	21
4.8	FITS Images as jpg from SkyView Virtual Observatory . . . . .	23
4.9	Axes Length Estimation Using Aladin v10.0 . . . . .	24
4.10	Pixel Extraction Using Aladin v10.0 . . . . .	25
4.11	Search for Background Objects in SIMBAD Astronomical Database . . . . .	27
4.12	Background Objects Visualization Within the Region of Interest . . . . .	28
5.1	Region of Interest in IRIS, AKARI, and WISE FITS Images . . . . .	30
5.2	Scatter Plot of Flux Densities against Wavelengths . . . . .	32
5.3	Contour Plots Showing Flux Density Distributions for Different Wavelengths . . . . .	32
5.4	Flux density Relationship Between Different Wavelengths of the Same Survey . . . . .	33
5.5	Contour Plots Showing Relationship Between Mass and Flux Distributions . . . . .	34
5.6	Gaussian Temperature Distributions in Different Surveys . . . . .	36
5.7	Gaussian Mass Distributions in Different Surveys . . . . .	37
5.8	Mass and Temperature Contour Plots in Different Surveys . . . . .	37
5.9	Emissivity and Average Temperature Relation for All Surveys . . . . .	39
5.10	Plot of Visual Extinction Against Temperature in IRIS and AKARI Data . . . . .	40
5.11	Background Objects and Mass Distribution in Different Surveys . . . . .	42

# Contents

<b>Acknowledgement</b>	viii
<b>Abstract</b>	ix
शोधसार	x
<b>List of Abbreviations</b>	xi
<b>List of Symbols</b>	xiii
<b>List of Tables</b>	xv
<b>List of Figures</b>	xv
<b>1 INTRODUCTION</b>	1
1.1 Background . . . . .	1
1.2 Objectives . . . . .	3
1.3 Significance of the Project . . . . .	3
1.4 Scope of the Project . . . . .	4
<b>2 LITERATURE REVIEW</b>	5
<b>3 THEORY</b>	8
3.1 Interstellar Medium . . . . .	8
3.2 Dust Structure Formation Around White Dwarf . . . . .	8
3.3 Dust Color Temperature Estimation . . . . .	9
3.4 Spectral Emissivity . . . . .	10
3.5 Visual Extinction and Optical Thickness . . . . .	11
3.6 Mass Estimation . . . . .	12
3.7 Jeans Criteria . . . . .	12
3.8 Inclination Angle . . . . .	14
<b>4 DATA AND METHODS</b>	15
4.1 Sources of Data . . . . .	15
4.1.1 SkyView Virtual Observatory . . . . .	15
4.1.2 Infrared Astronomical Satellite (IRAS) Survey . . . . .	16

4.1.3	AKARI Survey . . . . .	17
4.1.4	Wide-field Infrared Survey Explorer (WISE) . . . . .	18
4.1.5	SIMBAD Astronomical Database . . . . .	18
4.1.6	Gaia . . . . .	19
4.2	Methodology . . . . .	21
4.2.1	System Block Diagram . . . . .	21
4.2.2	Region of Interest . . . . .	21
4.2.3	Data Extraction and Reduction . . . . .	22
4.2.4	Data Analysis and Visualization . . . . .	25
<b>5</b>	<b>RESULT AND DISCUSSION</b>	<b>29</b>
5.1	Structure . . . . .	29
5.2	Flux Density Distribution . . . . .	31
5.3	Flux Density Relation . . . . .	33
5.4	Flux Density and Mass Relation . . . . .	33
5.5	Dust Color Temperature . . . . .	35
5.6	Dust Mass . . . . .	36
5.7	Jean's Mass . . . . .	38
5.8	Inclination Angle . . . . .	38
5.9	Spectral Emissivity . . . . .	39
5.10	Visual Extinction . . . . .	39
5.11	Background Sources . . . . .	40
<b>6</b>	<b>CONCLUSION AND FUTURE ENHANCEMENTS</b>	<b>43</b>
6.1	Conclusion . . . . .	43
6.2	Future Enhancements . . . . .	44
<b>Bibliography</b>		<b>45</b>

# Chapter 1

## INTRODUCTION

### 1.1 Background

Astrophysics is a branch of physics that is concerned with the application of methods and principles of physics to study astronomical objects and phenomena, (Maoz, 2016). The emissions from the astronomical bodies are within the electromagnetic (EM) spectrum (below 1 Hz to  $10^{25}$  Hz) which are crucial in the study of various properties of the objects such as luminosity, temperature, density, mass, chemical composition, emissivity and so on. Most astronomical objects don't emit in the visible spectrum but the study of other spectral regions within the EM spectrum, especially the IR spectrum (300 GHz – 430 THz), can be very useful for studying the properties and phenomena of such objects.

The observation and analysis of astronomical objects and phenomena using IR radiations is known as infrared astronomy. Frederick William Herschel, a German astrophysicist in early 1800, discovered IR light which became the foundation of infrared astronomy which began in the 1830s, (Cosmos, 2018). All objects emit IR radiations which are detected by IR detectors. Some of the IR telescopes that have been operating in space are the Infrared Astronomical Satellite (IRAS), Infrared Space Observatory (ISO), Midcourse Space Experiment (MSX), Spitzer Space Telescope, Akari, Herschel Space Observatory and Wide-field Infrared Survey Explorer (WISE). The IR data obtained from the surveys of these detectors are processed and analyzed to study astronomical objects and phenomena.

Before the 20th century, the Milky Way galaxy was thought to consist of stars in a vacuum. The first observational evidence that there was a general ISM between stars came from the photographic spectroscopy of spectroscopic binary stars in the early 20th century. Interstellar Medium (ISM) is the matter as well as radiation existing between the stellar systems or simply ISM is anything not in stars, (Osterbrock, 2000).

ISM primarily consists of Hydrogen (91%) followed by Helium (8.9%) with trace amounts of other gases (0.1%) like Carbon, Oxygen, and Nitrogen (Ferriere, 2001). Hydrogen and Helium are mainly the result of primordial nucleosynthesis while other metals (elements heavier than Hydrogen and Helium) are the consequence of stellar evolution processes. These gases in ISM exist in several

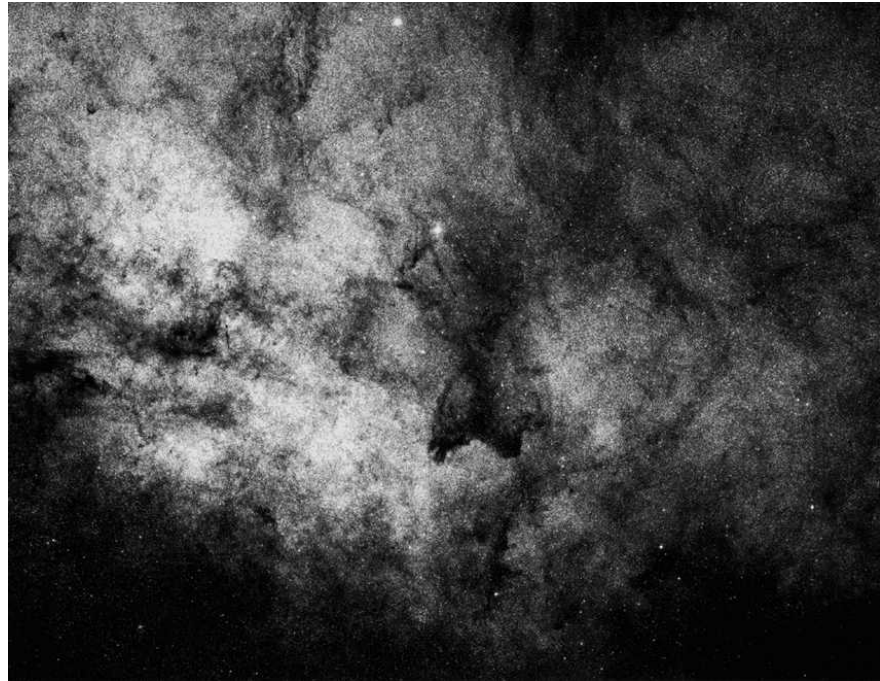


Figure 1.1: Dust Clouds in ISM

Source:(Carroll & Ostlie, 2014)

thermal phases depending on the local conditions of ionization, heating, and so on. In all phases, ISM has extremely low density. In cool, dense regions of ISM, the matter is mainly found in molecular forms with density up to  $10^6$  molecules per  $\text{cm}^3$  while in hot, diffuse regions, the matter is mostly in the ionized state with density as low as  $10^{-4}$  ions per  $\text{cm}^3$ . By mass, ISM is composed of 99% gases and 1% dust (Boulanger, Cox, & Jones, 2000). Stars form within the dense regions of ISM contributing to the molecular clouds, which is a type of interstellar cloud, the density and size of which results in the formation of molecules mostly  $\text{H}_2$ . These molecular clouds plenish the ISM with matter as well as energy through planetary nebulae, stellar winds, supernovae, and so on. This interaction between stars and ISM helps in determining the rate of depletion of gaseous contents of a galaxy and hence its lifespan of active star formation. Molecular clouds are in contrast to other regions of ISM which contain predominantly ionized gases.

On the other hand, even though ISM contains only 1% of dust, they play a crucial role in determining the chemical as well as thermodynamic distribution of ISM. These dust are generally solid microscopic particles of silicate, graphite, ice, and carbon-bearing compounds like hydrocarbons. They are usually  $0.1 - 1 \mu\text{m}$  in size. They are generally formed in the shells around evolved stars in AGB stages in stellar evolution while some fractions in circumstellar shells around supergiants, planetary nebulae, and white dwarfs. The majority of dust is formed in the cool, dense regions

of ISM by the process of accretion and coagulation while many other processes are still unknown (Tielens, 2005).

During the asymptotic giant branch (AGB) phase, a major fraction of mass is spread by the stars (0.6 - 10 M $\odot$ ) in the interstellar medium (ISM) in the form of dust. In the left phase of Post-Main Sequence evolution, these dust are found to be surrounding the White Dwarfs (WD). Some small fraction of dust is also formed in the circumstellar shells and cavities around WD which is usually a source of infrared (IR) excess. The formation and evolution of such IR dust structures are the results of high-pressure events and such structures are crucial in the study of interaction phenomena in ISM (Herwig, 2005).

## 1.2 Objectives

The objectives of the project can be divided as:

### General Objective

- To study the properties of dust structures around white dwarf WD0011-399 and the ongoing astrophysical phenomena.

### Specific Objectives

- To evaluate and analyze the IR flux density, dust color temperature, visual extinction, spectral emissivity, and dust mass of the isolated dust structure around the white dwarf WD0011-399.
- To study and visualize the relationship between various properties of the isolated dust structure.
- To predict whether the isolated structure is a probable star-forming region or not through the analysis of Jean's criteria.

## 1.3 Significance of the Project

The project has various significances, some of which are as follows:

- The dust properties around White Dwarf can preserve the record of fossils of the parent star and can also reveal prehistoric information helping light up the stellar evolution.

- The study of dust is also important to explore the chemistry of ISM. Infrared spectroscopy reveals the ongoing chemical as well as physical processes in ISM.
- Dust structures absorb the high energy radiation, like Ultraviolet, from the hot region of ISM and re-radiate the absorbed radiation as IR radiation. This implies that dust structures are important components in regulating the heating mechanism in ISM. Therefore, the study of dust grains is essential to understand the thermal distribution in ISM.
- Interstellar dust consists of Silicates and Carbon compounds which are the fundamental components for the formation of planetary systems, like the solar system. So, the study of such dust structures can provide crucial information regarding the evolution of planetary systems.

## 1.4 Scope of the Project

The project explores infrared data obtained from the IRAS survey at  $60\text{ }\mu\text{m}$  and  $100\text{ }\mu\text{m}$ , the AKARI survey at  $90\text{ }\mu\text{m}$  and  $140\text{ }\mu\text{m}$ , and the WISE survey at  $12\text{ }\mu\text{m}$  and  $22\text{ }\mu\text{m}$  to evaluate and analyze the properties of the dust structure around the white dwarf WD0011-399. These properties include dust color temperature, dust mass, IR flux density, inclination angle, visual extinction, spectral emissivity, and Jeans mass. However, the project doesn't encompass the following areas:

- The project cannot predict the exact stellar evolution model as the calculation of the nature of the perturbation in the surroundings is required to predict the exact model of stellar formation.
- The thermal properties of the dust within the selected regions along with the black body spectrum within dust clumps do not comply with the area of the study.
- The multi-wavelength band properties of dust structures cannot be studied using IR data.
- The project work involves the study of cold dust structures and doesn't include the study of any warm dust structures.

# Chapter 2

## LITERATURE REVIEW

The study of the isolated nebula in the southern hemisphere, at galactic longitude:  $286.127^\circ$  and latitude:  $-37.801^\circ$  is studied by (M. S. Paudel, 2013). The temperature variation in this nebula is 18.77 K to 24.51 K, with an average value of 21.78 K. The Gaussian-like variation of temperature across the major and minor diameter of the nebula is observed which suggests the nebula is less distracted from the external background sources. The mass of the gas in the nebula is found  $2.82 M_\odot$  and this mass is greater than the Jeans mass of the cloud  $0.48 M_\odot$  suggesting the possibility of a structure formation process in the future.

(M. S. Paudel, 2018) studied dust color temperature and dust mass of the two isolated dust nebula, size  $\sim 6.33 \text{ pc} \times \sim 1.98 \text{ PC}$ , and  $\sim 550 \text{ pc} \times \sim 319 \text{ pc}$  at galactic longitude:  $288.998^\circ$ , galactic latitude:  $-37.001^\circ$  and galactic longitude:  $280.744^\circ$ , galactic latitude:  $-35.699^\circ$  using the FIR images from IRAS satellite. The dust color temperature varies from 28.50 K to 9.20 K with an average value of 22.03 K for the first nebula and for the second nebula it varies from 40.90 K to  $25.15 \pm 9.60$  K with an average value of 33.99 7.82 K. From the large variation of temperature it is concluded that both nebula are not evolving independently or the role of discrete point sources in the field of nebula are playing the important for the shaping process of the nebula.

(Thapa, Paudel, & Pant, 2019) studied the dust color temperature, dust mass and other related properties of two new isolated nebula located at galactic latitude and longitude ( $353.01^\circ$ ,  $16.98^\circ$  &  $18.42^\circ$ ,  $1.98^\circ$  using the FIR images from IRAS satellite. The dust color temperature is found to lie in the range of 20.75 K to 35.90 K for the first region and 22.52 K to 45.63 K for the second region. The total mass of gas in the first structure is found to be  $20.99 M_\odot$  and  $5621.61 M_\odot$ . The Jean's mass is more than the mass of the gas, which are;  $180.99 M_\odot$  and  $6005.04 M_\odot$  respectively for the first and second nebula, indicating both nebulae might not be the star-forming region. Also, the study of inclination angle suggests that both nebulae are regularly and uniformly shaped.

A research paper by (Gautam & Chhatkuli, 2020) focused on the Planck function distribution in the FIR cavity around AGB2308+6058, an AGB star. The star was close to the Galactic plane at a galactic latitude of  $0.6^\circ$  resulting in a strong radiation field. The dust color temperatures were estimated within the range  $22.76 \pm 0.14$  K to  $23.55 \pm 0.29$  K with a low offset of 0.79 K suggesting

thermodynamic equilibrium in the cavity. The average temperature of the cavity was noted to be 22.14 K. A fluctuation in the distribution of the Planck function along both diameters of the FIR cavity was noticed, suggesting that the dust particles were oscillating non-uniformly and independently. Further, the dust mass was estimated as  $0.129 M_{\odot}$  with contour maps showing greater mass densities in the low-temperature regions thus supporting the cosmological principle. Also, the relation between visual extinction and dust color temperature was found to be linear with a high negative degree of correlation.

A similar study was done by (Jha & Aryal, 2018a) regarding the dust color temperature estimation of two FIR cavities located at R.A. (J2000) =  $14^h 41^m 23^s$ , Dec. (J2000) =  $-64^{\circ} 04' 17''$  and R.A. (J2000) =  $05^h 05^m 35^s$ , Dec. (J2000) =  $-69^{\circ} 35' 25''$  using IRAS (60 and 100  $\mu\text{m}$ ) and AKARI (90 and 140  $\mu\text{m}$ ) surveys. The dust color temperature of the first cavity located close to the galactic plane was found to lie in the range  $23.4 \pm 1.3$  K to  $24.1 \pm 1.4$  K with an offset of 0.7 K in IRIS maps while  $26.0 \pm 1.5$  K to  $28.2 \pm 1.6$  K, with an offset of 2.2 K in AKARI map. Similarly, for the second cavity far from the galactic plane, temperature ranges were  $22.2 \pm 1.2$  K to  $24.6 \pm 1.3$  K, with an offset of about 2.4 K and  $25.4 \pm 1.4$  K to  $29.7 \pm 1.7$  K, with a larger offset of 4.3 K in IRAS and AKARI maps respectively. Low offset suggested a higher probability of local thermodynamic equilibrium. Further, the difference in offset values of IRAS and AKARI suggested non-uniformity of the Planck function in the second cavity which led to the conclusion that the temperature of the second cavity may vary within the mean free path of the dust which causes deviation from the local thermodynamic equilibrium.

The dust color temperature, dust mass, and other physical properties of the dust cavity around the White Dwarf WD 0352-049 were studied by (M. Paudel, Bhandari, & Bhattacharai, 2021) using FIR images from SkyView Virtual Observatory. The study involved flux density, dust color temperature, and dust mass estimation. According to the study, the temperature of the whole cavity was estimated within the range of  $24.09 \pm 0.50$  K to  $21.87 \pm 0.61$  K with a fluctuation of 2.22 K and an average value of  $23.09 \pm 1.11$  K. The offset temperature of less than 5 K suggested that the dust in the cavity structure was less disturbed from external radiation sources and evolving independently while the average temperature led to the conclusion the dust is not a Cirrus-type cloud. The Gaussian distribution of the dust color temperature was visualized as well, suggesting the local thermodynamic equilibrium. Also, the variation of flux and temperature along both axes indicated the presence of thermal wind due to the WD near the center of the cavity. The study of Jean's criteria of the structure depicted the possibility of star formation activity within the structure and that of inclination angle concluded that the structure is uniformly shaped and regularly structured

from the morphological point of view.

(M. Paudel & Bhattacharai, 2021) studied the infrared properties of dust in a dust cloud located at galactic longitude:  $53.54^\circ$  and galactic latitude:  $0.04^\circ$  (RA:  $292.56^\circ$ , DEC:  $18.24^\circ$ , ICRS) surrounded by three Supernova Remnants G053.41+00.3, G053.9+00.2, and G053.1+00.3 using the FIR images from IRIS and AKARI data. The dust color temperature of dust cloud is obtained  $25.66 \text{ K} \pm 0.04 \text{ K}$  for IRIS data and  $17.74 \text{ K} \pm (3.42 \times 10^{-3}) \text{ K}$  for AKARI and mass of dust is  $28.45 \text{ M}_\odot$  in IRIS data and  $5.01 \times 10^4 \text{ M}_\odot$  in AKARI data. A large fluctuation of temperature, more than 10 K, in both IRIS and AKARI data is found, which implies the dust structure is far from the local thermodynamic equilibrium and might be due to the effect of background sources, such as Supernova Remnants, Pulsars, X-ray and gamma-ray sources, etc.

# Chapter 3

## THEORY

### 3.1 Interstellar Medium

The Interstellar Medium (ISM) is a collection of gas in ionic, atomic, and molecular form and dust between the stellar systems. The interstellar radiation field is the energy that occupies the same volume, in the form of electromagnetic radiation. ISM, by mass, is primarily composed of Hydrogen (70 %) followed by Helium (28 %) with a trace amount of heavier elements (1.5 %) such as Carbon, Oxygen, and Nitrogen. Hydrogen and Helium are mainly a result of primordial nucleosynthesis while the heavier elements are mostly a result of stellar evolution. The thermal pressures of these phases are in rough equilibrium with one another. Magnetic fields and turbulent motions also provide pressure in the ISM and are typically more important dynamics than the thermal pressure (Tielens, 2005).

During the lifetime of a star, depending on its total mass, much of the material born out may return to the ISM through stellar winds and explosive events. Subsequent generations of stars can thus be formed from these processed materials (Carroll & Ostlie, 2014). Objects with temperatures around 5 K to 340 K emit radiation in the FIR region which can be used to observe ISM gases where new stars are often formed. In the FIR region, stars are not especially bright, however, the emission from very cold objects (140 K or less) can be observed due to the thermal radiation of interstellar dust contained in molecular clouds. (Kundt, 2004)

### 3.2 Dust Structure Formation Around White Dwarf

Interstellar dust forms in the shells around evolved stars in the red giant branch (RGB) and asymptotic giant branch (AGB) stages during the evolution of the stars. During RGB and AGB phases, a major fraction of mass is spread by the stars ( $0.6 - 10 M_{\odot}$ ) in the ISM in the form of dust. In the left phase of Post-Main Sequence evolution, these dust are found to be surrounding the WDs. Some small fraction of dust is also formed in the circumstellar shells and cavities around WD which is usually a source of IR excess. The presence of circumstellar dust is revealed by its opacity and IR emission. The process of emissions into the ISM via stellar winds may be destructive, including

erosion and fragmentation in supernovas which generates shock waves, or constructive via mantle accretion and coagulation in more quiescent regions (Tielens, 2005).

These dust structures obscure relatively nearby regions in visible and UV regions and re-radiate the absorbed radiation in the FIR region thus contributing a major part (30 %) of the total luminosity of the Galaxy. The FIR radiation from dust removes the gravitational energy of collapsing clouds, allowing star formations. Dust is crucial for understanding the chemistry of ISM as it reduces the UV radiation which causes molecular dissociation thereby, providing a site of formation of the H<sub>2</sub> molecule which comprises most of the ISM. Moreover, dust controls the temperature of the ISM as it constitutes most of the elements contributing to the cooling process. On the other hand, it provides heat through photo-electrically ejected electrons from the grains (Böhm-Vitense, 1992). The formation and evolution of such IR dust structures are the results of high-pressure events and such structures are crucial in the study of interaction phenomena in ISM.

### 3.3 Dust Color Temperature Estimation

The dust temperature ( $T_d$ ) in each pixel of an FIR image can be obtained by considering the dust in a single beam is isothermal and that the observed ratio of 60 to 100  $\mu\text{m}$  emission is the result of blackbody radiation from the dust grains at  $T_d$  modified by a power-law emissivity spectral index (beta). The flux density of emission at wavelength  $\lambda_i$  is given by (Schnee, Ridge, Goodman, & Li, 2005),

$$F_i = \left[ \frac{2hc}{\lambda_i^3(e^{\frac{hc}{\lambda_i K T}} - 1)} \right] N_d \alpha \lambda_i^{-\beta} \Omega_i \quad (3.1)$$

where  $N_d$  represents the column density of dust grains,  $\alpha$  is a constant that relates the flux to the optical depth of the dust, and  $\Omega_i$  is the solid angle subtended at  $\lambda_i$  by the detector.

With the assumptions that the dust emission is optically thin at 60  $\mu\text{m}$  and 100  $\mu\text{m}$  (i.e.  $\tau_d \ll 1$ ) and that  $\Omega_{60} \approx \Omega_{100}$  (true for IRIS image), we can write the ratio, R, of the flux densities at 60  $\mu\text{m}$  and 100  $\mu\text{m}$  as,

$$R = \frac{F_{60}}{F_{100}} = \left[ \frac{60}{100} \right]^{-(3+\beta)} \left[ \frac{e^{\frac{T_{100}}{T_d}} - 1}{e^{\frac{T_{60}}{T_d}} - 1} \right] \quad (3.2)$$

Using the relation,  $T_{100} = \frac{hc}{\lambda_{100} k_B}$  and  $T_{60} = \frac{hc}{\lambda_{60} k_B}$  we get,  $T_{100} = 144K$  and  $T_{60} = 240K$ . Also, 1 can be dropped from both the numerator and denominator of equation 3.2 for smaller values of T.

So,

$$R = 0.6^{-(3+\beta)} \left[ \frac{e^{\frac{144}{T_d}}}{e^{\frac{240}{T_d}}} \right] \quad (3.3)$$

Taking the natural logarithm of equation 3.3 we obtain the value of  $T_d$  as,

$$T_d = \frac{-96}{\ln\{R \times 0.6^{(3+\beta)}\}} \quad (3.4)$$

For AKARI FIR data at 90  $\mu\text{m}$  and 140  $\mu\text{m}$ , equation 3.2 can be written as,

$$R = \frac{F_{90}}{F_{140}} = \left[ \frac{90}{140} \right]^{-(3+\beta)} \left[ \frac{e^{\frac{T_{140}}{T_d}} - 1}{e^{\frac{T_{90}}{T_d}} - 1} \right] \quad (3.5)$$

Using the relation,  $T_{140} = \frac{hc}{\lambda_{140}k_B}$  and  $T_{90} = \frac{hc}{\lambda_{90}k_B}$  we get,  $T_{140} = 103K$  and  $T_{90} = 160K$ . So,

$$R = 0.64^{-(3+\beta)} \left[ \frac{e^{\frac{103}{T_d}}}{e^{\frac{160}{T_d}}} \right] \quad (3.6)$$

Taking the natural logarithm of equation 3.6 we obtain the value of  $T_d$  as,

$$T_d = \frac{-57}{\ln\{R \times 0.6^{(3+\beta)}\}} \quad (3.7)$$

For WISE FIR data at 12  $\mu\text{m}$  and 22  $\mu\text{m}$ , equation 3.2 can be written as,

$$R = \frac{F_{12}}{F_{22}} = \left[ \frac{12}{22} \right]^{-(3+\beta)} \left[ \frac{e^{\frac{T_{22}}{T_d}} - 1}{e^{\frac{T_{12}}{T_d}} - 1} \right] \quad (3.8)$$

Similarly,  $T_{12} = \frac{hc}{\lambda_{12}k_B}$  and  $T_{22} = \frac{hc}{\lambda_{22}k_B}$  we get,  $T_{12} = 1199K$  and  $T_{22} = 654K$ . So,

$$R = 0.64^{-(3+\beta)} \left[ \frac{e^{\frac{654}{T_d}}}{e^{\frac{1199}{T_d}}} \right] \quad (3.9)$$

Taking the natural logarithm of equation 3.9 we obtain the value of  $T_d$  as

$$T_d = \frac{-545}{\ln\{R \times 0.6^{(3+\beta)}\}} \quad (3.10)$$

### 3.4 Spectral Emissivity

According to (Dupac et al., 2003), the inverse relation between the emissivity index  $\beta$  and dust color temperature  $T_d$  is,

$$\beta = \frac{1}{\delta + \omega T_d} \quad (3.11)$$

where parameters  $\delta$  and  $\omega$  depend on the dust grain properties like composition, size, compactness, and so on and have values  $\delta = 0.40 \pm 0.02$  and  $\omega = 0.0079 \pm 0.0005 K^{-1}$

For pure black body,  $\beta = 0$ ,

For amorphous layer-lattice matter,  $\beta \sim 1$  and

For metals and crystalline dielectrics  $\beta \sim 2$ .

### 3.5 Visual Extinction and Optical Thickness

Because the dust is optically very thin i.e.:  $\tau_d \ll 1$ , the dust optical depth at  $100 \mu\text{m}$  can be calculated as given by (Wood, Daugherty, & Myers, 1994),

$$\tau_{100} = \frac{F_{100\mu\text{m}}}{B(\lambda, T_d)} \quad (3.12)$$

where  $F_\lambda(100)$  is the observed flux at wavelength of  $100 \mu\text{m}$  and  $B_\lambda(\lambda, T_d)$  is the Planck function given by,

$$B(\lambda, T) = \frac{2hc^2}{\lambda^5} \left[ \frac{1}{e^{\frac{hc}{\lambda k_B T}} - 1} \right] \quad (3.13)$$

is the spectral emissive power per unit area per unit solid angle for a particular wavelength of radiation.

Interstellar extinction is the dimming of distant objects due to the presence of dust in the ISM along the line of sight (LOS). Visual extinction can be defined as the difference between the magnitude with and without interstellar extinction and is expressed as,

$$A(\lambda) = m_{attenuated} - m_0 = 2.5 \log_{10} \left[ \frac{F_\lambda^0}{F_\lambda^a} \right] \quad (3.14)$$

Where  $F_\lambda^a$  is the dust attenuated observed flux,  $m_{attenuated}$  is the corresponding apparent magnitude of the object, and  $F_\lambda^0$  is the flux that would have been observed if there would have been no attenuation from dust and  $m_0$  is the corresponding apparent magnitude of the object. Let the optical thickness be  $\tau(\lambda)$ , then

$$F_\lambda^a = F_\lambda^0 e^{-\tau(\lambda)} \quad (3.15)$$

Combining equations 3.14 and 3.15 we obtain,

$$A(\lambda) = (2.5 \log_{10} e) \tau(\lambda) \quad (3.16)$$

The relation between extinction and optical thickness is linear with slope ( $2.5 \log_{10} e$ ) (Schnee et al., 2005). This equation gives a very high value of optical thickness for  $100 \mu\text{m}$  and  $140 \mu\text{m}$  wavelength which doesn't comply with our assumption that the dust is optically thin for  $100 \mu\text{m}$  and  $140 \mu\text{m}$  wavelength.

Assuming optically thin emission, the value of V - band extinction is as modified by Wood et. al (Wood et al., 1994) for  $100 \mu\text{m}$  flux is given by,

$$A(\lambda) = 15.078(1 - e^{\frac{-\tau_{100}}{641.3}}) \quad (3.17)$$

## 3.6 Mass Estimation

First, the value of flux density,  $F_\lambda$ , at  $100 \mu\text{m}$  is determined then the dust mass can be calculated as suggested by (Hildebrand, 1983),

$$M_d = \frac{4a\rho}{3Q_\lambda} \left[ \frac{F_\lambda D^2}{B(\lambda, T)} \right] \quad (3.18)$$

where  $a$  = weighted grain size ( $0.1 \mu\text{m}$ )

$\rho$  = grain density ( $3000 \text{ kg m}^{-3}$ )

$Q_\lambda$  = grain emissivity at wavelength  $\lambda$  ( $0.001$  for  $100 \mu\text{m}$ )

$B(\lambda, T)$  = Planck's function

Substituting the values we get the reduced equation as suggested by (Young, Phillips, & Knapp, 1993),

$$M_d = 0.4 \left[ \frac{F_\lambda D^2}{B(\lambda, T)} \right] \quad (3.19)$$

FIR emission is measured from the  $100 \mu\text{m}$  IRAS images for the derivation of the dust mass because the longer wavelength measurements give us more precise dust masses due to the characteristics of the Planck function.

## 3.7 Jeans Criteria

According to the Virial theorem, the kinetic energy  $\langle T \rangle$  of a stable system must be equal to the negative half of its gravitational potential energy  $\langle U \rangle$ . Mathematically, it is expressed as,

$$\langle 2T \rangle + \left\langle \sum_{i=1}^n F_i, r_i \right\rangle = 0 \quad (3.20)$$

Since  $\langle \sum_{i=1}^n F_i, r_i \rangle = \langle U \rangle$  so,

$$\langle T \rangle = -\frac{1}{2} \langle U \rangle \quad (3.21)$$

It implies that there must exist a critical mass of a molecular cloud to be stable or to collapse. The process of collapsing a molecular cloud due to its gravity is known as gravitational collapse. For the cloud to be stable, it must be in hydrostatic equilibrium. If the internal pressure of the gas is greater than the gravitational force then the mass will collapse and instability occurs which is known as Jeans instability. Jeans mass, named after British physicist James Jeans, is the critical mass required for Jean's stability. It depends on two thermodynamic parameters; pressure ( $P$ ) and density ( $\rho$ ) (Carroll & Ostlie, 2014). The relation can be expressed as,

$$M \propto P^a \rho^b G^c \quad (3.22)$$

where  $G$  = universal gravitational constant and  $a, b, c$  are constants to be determined.

On determining the values of  $a, b$ , and  $c$  using the dimensional method we get Jean's mass as,

$$M_J = \frac{K P^{\frac{3}{2}}}{\rho^2 G^{\frac{3}{2}}} \quad (3.23)$$

where  $K$  is proportionality constant which depends on the nature of perturbation. The perturbation depends on the speed of acoustic waves and adiabatic index.

For slow varying perturbation,

$$K = \frac{4}{3} \pi^{\frac{5}{2}} \quad (3.24)$$

The molecular clouds are extremely cold, the equation of state for non-degenerate gas can be applied as,

$$P = \frac{\rho k_B T}{\mu m_H} \quad (3.25)$$

As no ionization takes place in the molecular cloud, so  $m_H = 1$ . Thus,

$$P = \frac{\rho k_B T}{\mu} \quad (3.26)$$

Once the size and temperature of the region are known density can be calculated as,

$$\rho = \left( \frac{3}{4\pi} \right)^{\frac{2}{3}} \left[ \frac{k_B T_d}{m_H G R^2} \right] \quad (3.27)$$

Jean's mass can thus be calculated as,

$$M_J = K \left( \frac{k_B T}{\mu G} \right)^{3/2} \frac{1}{\rho^{1/2}} \quad (3.28)$$

The diameter of the gas is termed as Jean's length ( $\lambda_J$ ) which can be calculated as,

$$\lambda_J = 2K \left( \frac{3}{4\pi} \right)^{1/3} \left( \frac{k_B T}{\mu \rho G} \right) \quad (3.29)$$

where  $k_B$  = Boltzmann's constant

$T$  = temperature of the molecular cloud

$\mu$  = mass per particle in the cloud

$m_H$  = mass of proton (in kg)

Jeans length gives the critical size of the cloud at a given temperature for Jeans stability.(Karttunen, Kröger, Oja, Poutanen, & Donner, 2007)

## 3.8 Inclination Angle

The inclination angle ( $i$ ) is the angle between the LOS and the normal vector of the plane of the structure. This can be estimated by using (Holmberg, 1946) formula,

$$\cos^2 i = \frac{\left(\frac{b}{a}\right)^2 - q^*{}^2}{1 - q^*{}^2} \quad (3.30)$$

where  $(b/a)$  is the ratio of minor to major diameter and  $q^*$  is the intrinsic flatness of the structure.

The intrinsic flatness is closely related to nebula morphology. It depends on the amount of molecular hydrogen and the dust. The dust grains obtain energy from the heating due to the photoelectric effect and low-energy cosmic rays. Due to this vibrational degree of freedom is greatly enhanced. This makes the cloud to be flat (the opening angle gradually increases with the dilution and vibrational excitation of the dust). Thus the range of the intrinsic flatness of the cloud is taken between 0.13 to 0.33. (Haynes & Giovanelli, 1984)

# Chapter 4

## DATA AND METHODS

### 4.1 Sources of Data

#### 4.1.1 SkyView Virtual Observatory

SkyView is a Virtual Observatory on the Net generating images of any part of the sky at wavelengths in all regimes from Radio to Gamma-Ray. Over 100 survey datasets are currently available. The SkyView library referenced here is used as the basis for the SkyView website but is designed for individual use by researchers as well.

SkyView's approach to access surveys is distinct from most other toolkits. Rather than providing links to the original data, SkyView attempts to immediately re-render the source data in the user-requested reference frame, projection, scaling, orientation, etc. The library includes a set of geometry transformation and mosaicking tools that may be integrated into other applications independent of SkyView (Mcglynn & White, 1997).

The screenshot shows the "SkyView Query Form" interface. At the top, there are links for "Home", "Query Form", and "Help". Below these are buttons for "Initiate request", "Submit", "Reset forms", "Reset", and "Display results in new window". A section titled "Required Parameters:" contains fields for "Coordinates of Source" (J2000 coordinates: 16 17 24, -39 13 14.7) and "Surveys" (a dropdown menu). To the right, there are sections for "Common Options" (Coordinate system: J2000, Projection: Gnomonic (Tan), Image size (pixels): 500, Image Size (degrees): 0.5, Use 4-byte floating point values for FITS file, Initiate request, Submit Request) and "Other Options" (Brightness scaling: Histogram Equalization (HistEq), Name Resolver: SIMBAD-NED, Pixel Resampling: Default (usually NN), Edge Reduction: Survey default, Rotation (degrees): 0, Smoothing: 1, Color Table: a large grid of color palettes). The bottom of the form has "Clear Survey Selections" and "Initiate request, Submit Request" buttons.

Figure 4.1: SkyView Query Form Interface

Source: ([skyview.gsfc.nasa.gov/current/cgi/query.pl](http://skyview.gsfc.nasa.gov/current/cgi/query.pl))

#### 4.1.2 Infrared Astronomical Satellite (IRAS) Survey

IRAS was a joint project of the National Aeronautics and Space Administration (NASA), Netherlands Agency for Aerospace Programmes (NIVR), and Science and Engineering Research Council (SERC) first launched on 25 January 1983 (C. A. Beichman & Cheste, 1988). It was the first space telescope to perform a survey of the entire night sky at infrared wavelengths. The IRAS Sky Survey Atlas (ISSA) is a set of Flexible Image Transport System (FITS) images of the infrared sky at 12, 25, 60, and 100  $\mu\text{m}$  made from co-added IRAS survey data at moderate resolution (Schmadel, 2003). These FITS are digital file formats useful for the storage, transmission, and processing of data, formatted as multi-dimensional arrays (like 2D images) or tables. The FITS format is most commonly used in astronomy. The FITS standard was designed specifically for astronomical data and includes provisions such as describing photometric and spatial calibration information, together with image origin metadata.



Figure 4.2: IRAS Satellite

Source: ([www.jpl.nasa.gov/missions/infrared-astronomical-satellite-iras](http://www.jpl.nasa.gov/missions/infrared-astronomical-satellite-iras))

For this project the ISSA FITS images at 60 and 100  $\mu\text{m}$  are obtained from SkyView Virtual Observatory. These FITS images contain flux density data at a given wavelength which are then imported in Aladin v10.0 followed by non-redundant data extraction of each pixel. This new generation of IRAS images, called IRIS, benefits from a better zodiacal light subtraction, from calibration and zero level compatible with Diffuse Infrared Background Experiment (DIRBE), and

a better destriping (removal of stripes or streaks from images). It includes well-calibrated point sources and the diffuse emission calibration at scales smaller than 1 degree, corrected for the variation of the IRAS detector responsively with scale and brightness. The uncertainty on the IRIS calibration and zero level are dominated by the uncertainty on the DIRBE calibration and the accuracy of the zodiacal light model (Miville-Deschénes & Lagache, 2005).

#### 4.1.3 AKARI Survey

AKARI (formerly known as ASTRO-F) is an infrared astronomy telescope developed by the Japanese Aerospace Exploration Agency (JAXA) to perform an all-sky survey with better spatial resolution and wider wavelength coverage than IRAS. It maps the entire sky in six infrared bands from 9 to 180  $\mu\text{m}$  (near, mid, and far-IR regions). AKARI is now in its Post-Helium phase, where imaging and spectroscopic features are available within 1.8 to 5.5  $\mu\text{m}$  (Bertout et al., 2010).



Figure 4.3: AKARI Satellite

Source: ([www.isas.jaxa.jp/en/missions/spacecraft/past/akari.html](http://www.isas.jaxa.jp/en/missions/spacecraft/past/akari.html))

Similar to IRAS, the AKARI data are also obtained in the form of FITS images from SkyView Virtual Observatory. However, the AKARI survey data are taken only from the AKARI-S (90  $\mu\text{m}$ ) and AKARI-L (140  $\mu\text{m}$ ).

#### 4.1.4 Wide-field Infrared Survey Explorer (WISE)

Wide-field Infrared Survey Explorer is a NASA astronomy telescope operating in the infrared region. It was launched in 2009 and since has discovered numerous star clusters, remote galaxies, asteroids, and other astronomical objects. WISE performed an all-sky survey with images in 3.4, 4.6, 12, and 22  $\mu\text{m}$  wavelength range bands (Wright et al., 2010). However, for this specific project, only the images at 12 and 22  $\mu\text{m}$  were considered. The survey images are available as FITS images in SkyView Virtual Observatory.

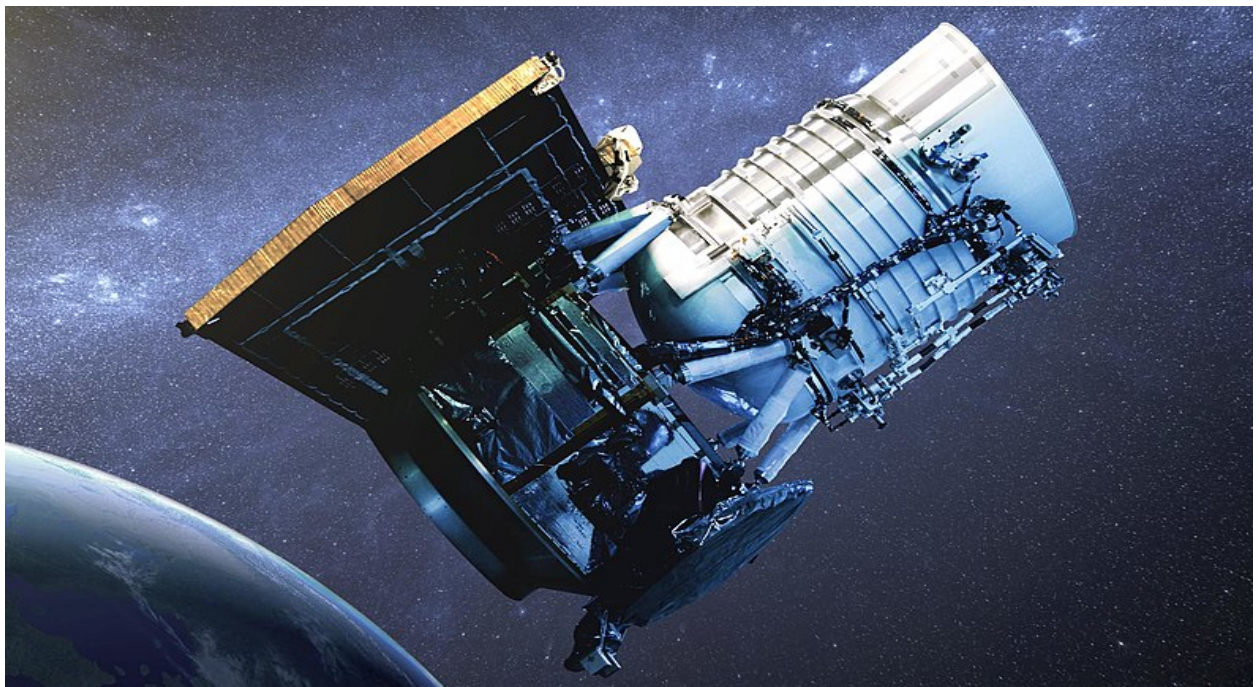


Figure 4.4: WISE Satellite

Source: ([photojournal.jpl.nasa.gov/jpeg/PIA17254.jpg](http://photojournal.jpl.nasa.gov/jpeg/PIA17254.jpg))

#### 4.1.5 SIMBAD Astronomical Database

SIMBAD stands for Set of Identifications, Measurements, and Bibliography for Astronomical Data. It is an astronomical database that provides basic data, cross-identifications, bibliography, and measurements for astronomical objects outside the solar system. The astronomical objects specifically excluded are the Sun and Solar System bodies. It is maintained by the Centre de données astronomiques de Strasbourg (CDS), Strasbourg (Wenger et al., 2000). The specificity of the Simbad database is to organize the information per astronomical object, thus offering a unique perspective on astronomical data, which is done through a careful cross-identification of objects from catalogs,

lists, and journal articles. SIMBAD can be queried by the object name, coordinates, and various criteria along with lists of objects and scripts.

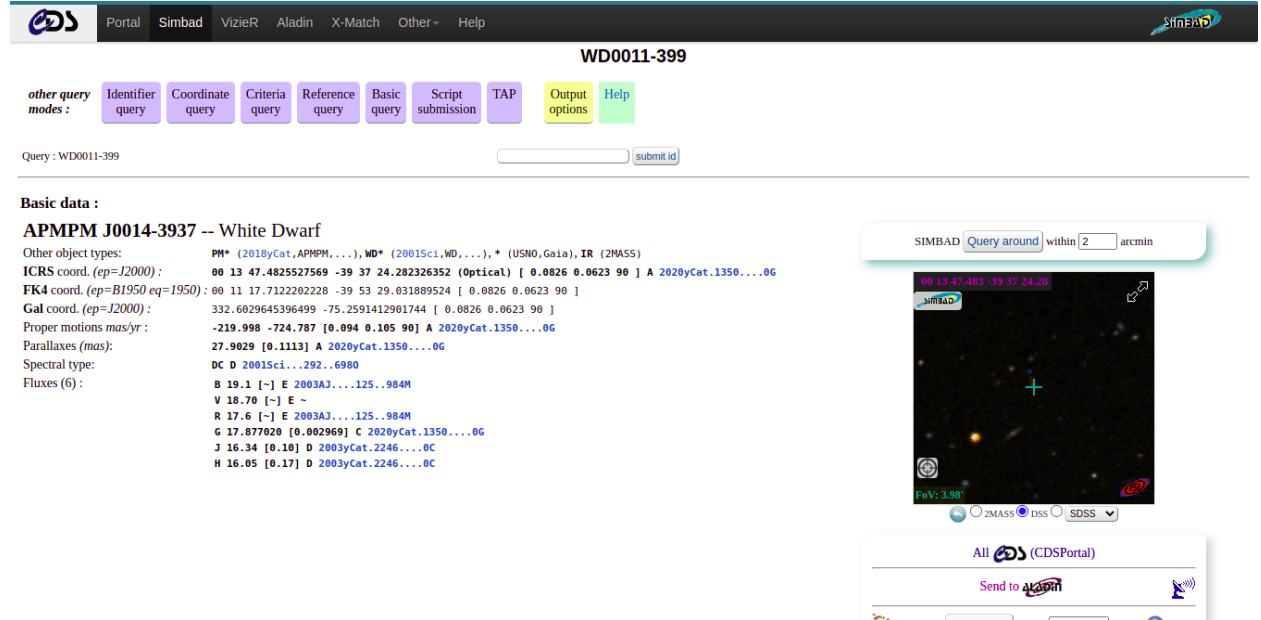


Figure 4.5: Simbad Query Interface

Source: ([simbad.cds.unistra.fr/simbad/sim-fid](http://simbad.cds.unistra.fr/simbad/sim-fid))

SIMBAD provides an easy and versatile way for searching astronomical objects. In addition to the astronomical body under search, it also provides a method for obtaining other astronomical objects within specified neighborhood radius. SIMBAD astronomical database was utilized for obtaining the data regarding the object under research along with the objects around it. SIMBAD database gives access to various data such as object type, angular distance, coordinates (in ICRS, Galactic, FK4, and FK5), coordinate maximum and minimum errors, flux values with various filters along with flux errors, proper motion, parallaxes along with parallax errors and many more. Moreover, the SIMBAD database was also used for validating candidate white dwarfs and obtaining their coordinates.

#### 4.1.6 Gaia

Gaia is a space observatory of the European Space Agency (ESA) launched in 2013 to make the largest and most precise 3D map of the Milky Way galaxy by surveying an unparalleled 1% of the galaxy's population of 100 billion stars. It detects and measures the motion of each star in its orbit around the center of the galaxy (Brown et al., 2021). Studying this motion allows us to study various astrophysical phenomena from the time, to when the Galaxy was first forming. By

constructing a detailed map of the stars, Gaia provides a crucial tool to study the formation of our galaxy.

Gaia database was utilized for the calculation of distance using the parallax method. The parallax method determines the distance between any nearby astronomical object against background objects by measuring an apparent shift in the position of the astronomical body. Gaia Archive contains the deduced positions, parallaxes, proper motions, radial velocities, and brightness data of more than 100 million stars. The early installment of the third Gaia data release, Gaia EDR3, contains astrometry and photometry, complemented with radial velocities from Gaia DR2 after the removal of a small number of spurious entries. Using Advanced Data Query Language (ADQL) data regarding RA, Dec., parallax, parallax error, proper motion of RA and Dec., and proper motion errors in RA and Dec. were obtained from the Gaia EDR3 database. The parallax and parallax error data were then used for measuring the distance.

The screenshot shows the Gaia ADQL interface. At the top, there's a navigation bar with links for HOME, SEARCH, VISUALISATION, and HELP. Below that is a sub-navigation bar with links for Basic, Advanced (ADQL), and Query Results. The main area has a search bar with the text 'gala' and a dropdown menu. To the right of the search bar is a 'Query examples' section. The central part of the interface is a code editor containing an ADQL query:

```

1 SELECT ra, dec, parallax, parallax_error, pmra, pmra_error, pmdec, pmdec_error
2 FROM gaiaedr3.gaia_source
3 WHERE
4   (
5     (ra BETWEEN 3.6 AND 4.2 AND dec BETWEEN -39.2 AND -38.9)
6   )

```

Below the code editor is a note: "Ctrl+Space for query autocomplete". To the right of the code editor are 'Reset Form' and 'Submit Query' buttons. Below the code editor is a table showing two jobs:

Status	Job	Creation date	Num. rows	Size
<input checked="" type="checkbox"/>	<input checked="" type="checkbox"/> 1653814578991O	29-May-2022, 14:41:18	1229	49 KB
<input checked="" type="checkbox"/>	<input type="checkbox"/> 1653814519540O	29-May-2022, 14:40:19	0	1 KB

At the bottom of the interface are buttons for 'Download format: VOTable', 'Apply jobs filter', 'Filter this session', 'Select all jobs', and 'Delete selected jobs'. A footer at the bottom right indicates the version: '(v3.0.1)'.

Figure 4.6: Gaia ADQL Interface

Source: ([gea.esac.esa.int/archive/](http://gea.esac.esa.int/archive/))

## 4.2 Methodology

### 4.2.1 System Block Diagram

The workflow of the project as depicted below involves searching for regions of interest, extraction and reduction of data, and calculation and visualization of dust properties using various tools and techniques.

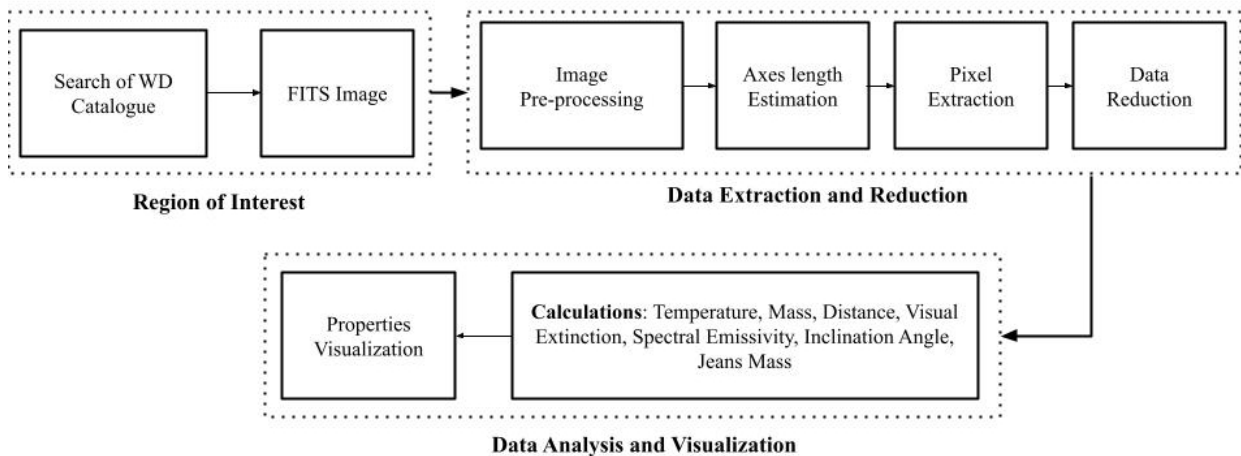


Figure 4.7: System Block Diagram (Research Plan)

### 4.2.2 Region of Interest

#### Search of White Dwarf Catalogue

A series of methods were applied to locate an appropriate region of interest. Initially, the white dwarfs along with candidate white dwarfs were located using published white dwarf catalogs and databases such as Montreal White Dwarf Database (MWDD) (Dufour et al., 2016), Villanova Catalog of Spectroscopically Identified White Dwarfs (McCook & Sion, 1999). and SIMBAD Astronomical Database-CDS. Furthermore, these databases were very useful in the verification of white dwarf candidates along with other astronomical bodies around them. After the verification of the candidates as white dwarfs, their coordinates were used to perform the search of isolated dust structures around the white dwarfs, which was done in SkyView Virtual Observatory. The parameters used during the SkyView survey were as follows:

Table 4.1: Parameters and their Values for SkyView Query Form

Parameters	Values
Survey Selection	<b>IRAS</b> : IRIS 60, IRIS 100 <b>AKARI</b> : AKARI WIDE-S, AKARI WIDE-L <b>WISE</b> : WISE 12, WISE 22
Coordinate System	J2000
Image Size	<b>IRIS</b> : $0.5^\circ$ , 25 pixels <b>AKARI</b> : $0.18^\circ$ , 30 pixels <b>WISE</b> : $0.1^\circ$ , 30 pixels
Brightness Scaling	Histogram Equalization (HistEq)
Color Table	Stern Special

## FITS Image

After submitting the query form, the images were analyzed to locate isolated dust structures around the white dwarf. When isolated dust structures on all the surveys were located clearly, the FITS images of all surveys were downloaded. The image size parameters were adjusted for different surveys depending on the pixel visibility as different surveys have regions visible at different sizes due to variations in the wavelength of observations.

### 4.2.3 Data Extraction and Reduction

#### Image Preprocessing

After obtaining the FITS images of the region of interest in various surveys, they were preprocessed in Aladin v.10.0. The pixel values were adjusted depending on the visibility of the regions. For images containing many white pixels, the pixel values were reversed. Although it is not mandatory, it makes the visibility better. Then the contours were generated for locating the regions with approximately the same flux density values. The levels of contours were generated as per convenience. A smoothing level of 2 was used along with inbuilt noise reduction. The contour properties were adjusted from the pixel value histogram such that the inner regions were enclosed. Since the outer contours were of not much importance they were considered even when not enclosed.

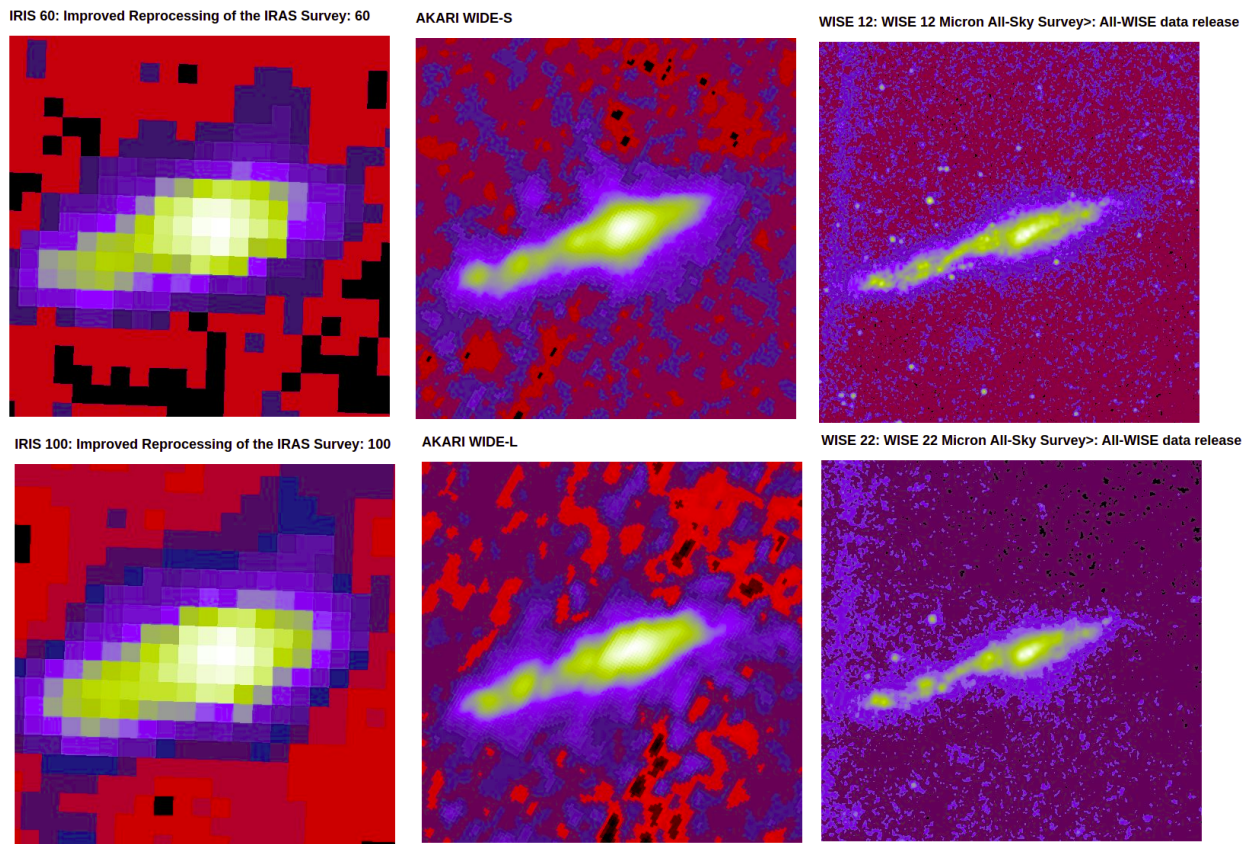


Figure 4.8: FITS Images as jpg from SkyView Virtual Observatory

Source: ([skyview.gsfc.nasa.gov/current/cgi/query.pl](http://skyview.gsfc.nasa.gov/current/cgi/query.pl))

### Axes Length Estimation

The minimum and maximum flux density values (pixel values) were located by observing the minimum and maximum color values among the pixels and then tagged using the tag marker of the interface. The major axis and minor axis were also calculated with the distance selector of the software environment such that they both intersect at the pixel with maximum flux density.

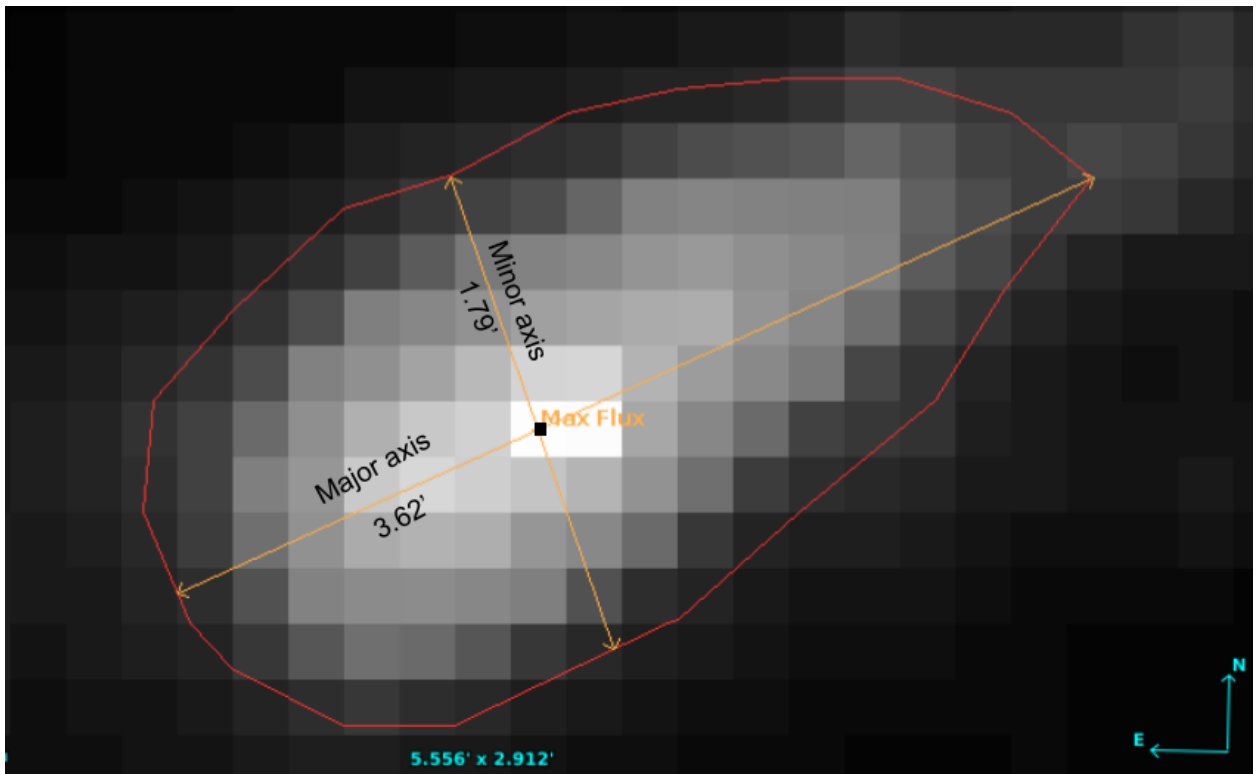


Figure 4.9: Axes Length Estimation Using Aladin v10.0

## Pixel Extraction

The flux density values along with pixel location and coordinates of each pixel were extracted using the pixel extraction feature of the interface. When extracting the pixels it was made sure that the pixels values were non-redundant. Although the user interface had much more functionalities, only the task-specific functionalities were used. After pixel extraction, the data of all the pixels were copied into .xlsx format. In addition to that, the interface also has data exporting features in JSON, TSV, and text formats.

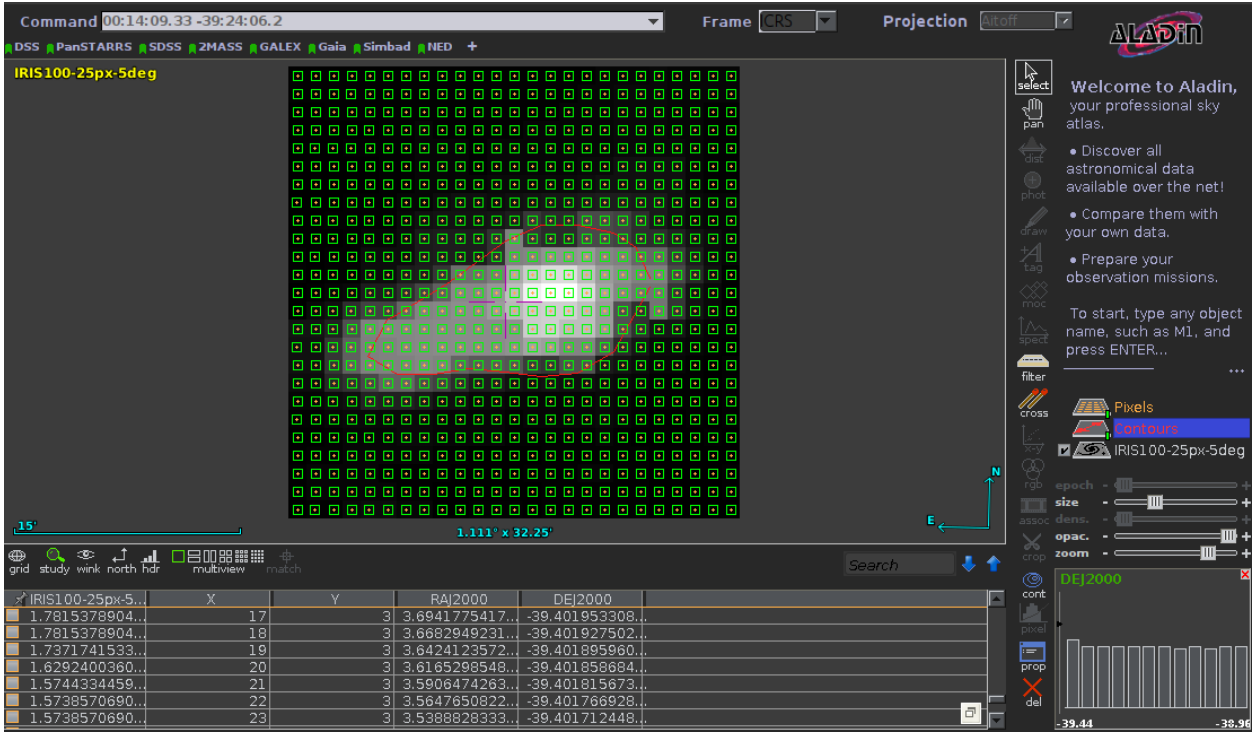


Figure 4.10: Pixel Extraction Using Aladin v10.0

## Data Reduction

Before exporting the data into .csv format there were a few amendments to be done. The coordinates of the pixels were in the format of hr, min, and sec for R.A. and deg, arcmin, and arcsec for Dec. They both were converted into degrees by basic unit conversion formulae.

$$\begin{aligned}
 1 \text{ hour} &= 60 \text{ minutes} = 3600 \text{ seconds} \\
 1 \text{ degree} &= 60 \text{ arcminutes} = 3600 \text{ arcseconds} \\
 1 \text{ degree} &= 15 \text{ hours}
 \end{aligned} \tag{4.1}$$

### 4.2.4 Data Analysis and Visualization

The post-processing part of the project was all done in Python Notebook as it has easy and efficient data manipulation and visualization features. First, the .csv data files were read as pandas dataframe. Then the properties of the dust structure such as Dust color temperature, dust mass, Jean's mass, spectral emissivity, visual extinction, and inclination angle were calculated as per the theory for IRIS, AKARI, and WISE data. They were then visualized using the matplotlib module of Python. More specifically, plots such as scatter plots, tricontour plots, hexbin plots, histogram plots, and best-fit plots were done for various data to visualize and analyze different

properties of the region of interest. Also, the relationship between various properties along with their distribution was visualized using various plots. Only the data of the region of interest was taken by manually eliminating the values greater than the contour value enclosing the region of interest. This allowed us to visualize only the properties of the region of interest.

## Distance Calculation

The data required for the project are regarding RA (`ra`), Dec. (`dec`), parallax (`parallax`), parallax error (`parallax_error`), proper motion of RA (`pmra`), and Dec. (`pmdec`) and proper motion errors in RA (`pmra_error`) and Dec. (`pmdec_error`). Then advanced query is done within a range of RA and Dec. using Advanced Data Query Language (ADQL) as:

```
SELECT ra, dec, parallax, parallax_error, pmra, pmra_error, pmdec, pmdec_error
FROM gaiaedr3.gaia_source
WHERE
(
    (ra BETWEEN 312.18 AND 313.18 AND dec BETWEEN -22.42 AND -21.82)
)
```

After obtaining the data from Gaia Archive in `.csv` format, the data was preprocessed for ease of calculation. The coordinates (RA and Dec.) were changed into degrees and data with negative parallaxes, parallaxes greater than 10 and less than 0.5 were removed. Then the range of the parallax was calculated as:

$$\text{Range} = (\text{Mean} - \text{SD}, \text{Mean} + \text{SD}) \quad (4.2)$$

Then the data within Range 0 and 1 were taken to remove the nearest and farthest objects. The relative error in parallax was calculated as:

$$\text{Relative Parallax Error} = \frac{\text{Parallax}}{\text{Parallax Error}} \quad (4.3)$$

Using the above formula the data having relative parallax error greater than 5 i.e. parallax error greater than 20% were removed. Then the distance was calculated using the formula:

$$\text{Distance} = \frac{1000}{\text{Mean Parallax}} \quad (4.4)$$

## Background Sources Visualization

The data regarding the background sources were obtained from the SIMBAD astronomical dataset. In SIMBAD database GUI under coordinate query, the coordinates (RA(J2000): 00 15 17.24, Dec.(J2000): -39 13 14.7) along with the coordinate system (ICRS) and radius (20') within which objects are to be searched was given as input and the query was submitted. The radius was chosen as half of the angular size given as input in the SkyView query form. Then a list of objects found within the given radius assuming a given coordinate as the center was obtained which was the required data. The data was then obtained in .csv format from the CDS portal.

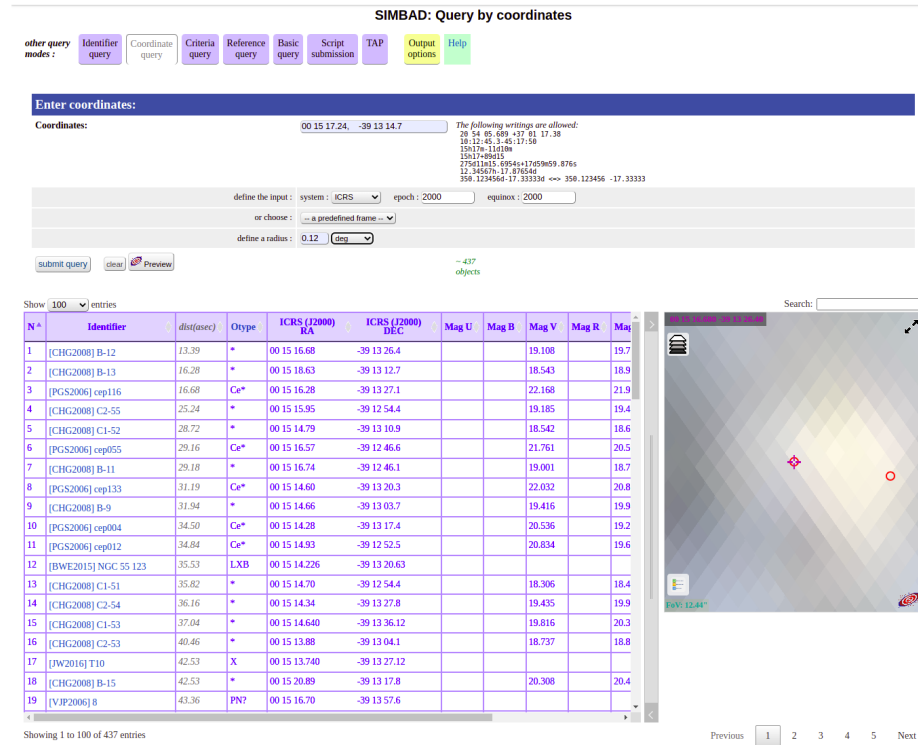


Figure 4.11: Search for Background Objects in SIMBAD Astronomical Database

Source: ([simbad.cds.unistra.fr/simbad/sim-fid](http://simbad.cds.unistra.fr/simbad/sim-fid))

The obtained data was then visualized using the `matplotlib` module of Python by plotting the background objects against the coordinates as shown in Figure 4.12. The types of astronomical objects visualized within the region were included in the legends for ease of visualization.

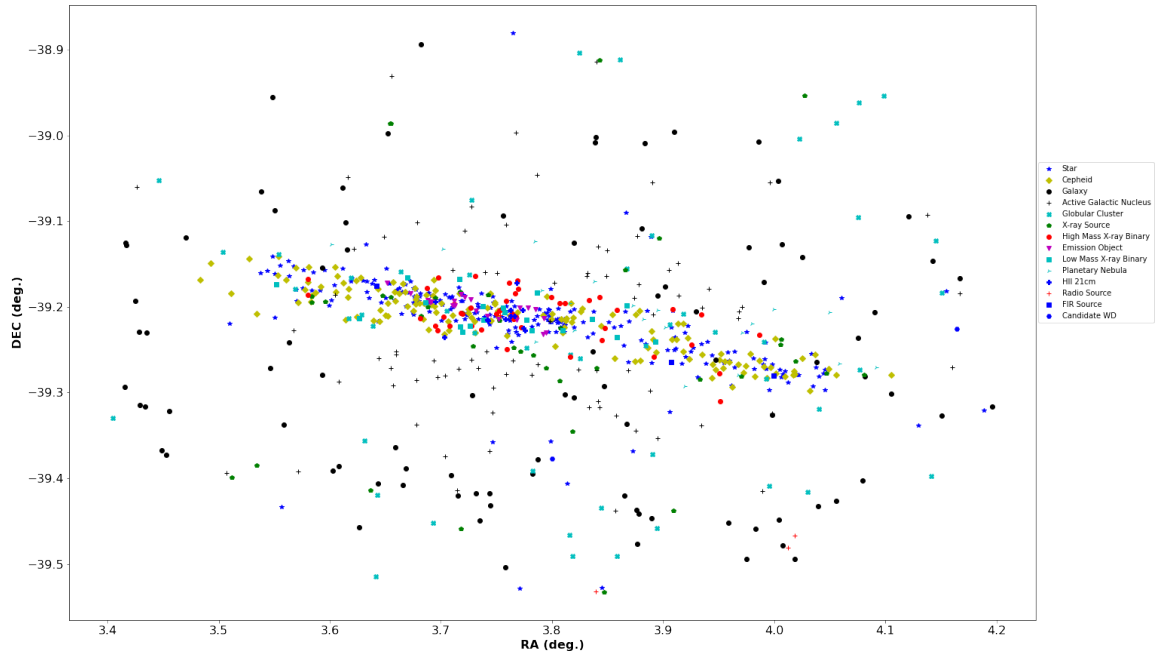


Figure 4.12: Background Objects Visualization Within the Region of Interest

# Chapter 5

## RESULT AND DISCUSSION

### 5.1 Structure

The structural visualization of the FITS image of the dust structure was done in Aladin v10.0. The pixel color values were adjusted for clear visualization and different levels of contours were drawn around the cavity distinguishing the cavity region from the rest parts of the image. Contour maps also aid in the distinction of regions with minimum and maximum flux densities. Only one minima and maxima were observed within the region of interest. The pixel location of maximum flux density acts as a point of intersection of the major and minor axes of the region of interest. In IRIS (100  $\mu\text{m}$ ), AKARI (140  $\mu\text{m}$ ), and WISE (22  $\mu\text{m}$ ) FITS images, the maximum flux densities were 47.45, 129.94 and 166.33 MJysr $^{-1}$  respectively. On drawing the longest and shortest axes passing through the maximum flux density pixel and joining the opposite ends of the contour the obtained major axis and minor axis in the IRIS FITS image were 19.01' and 9.64' respectively thus the angular dimension of the region of interest was 19.01'  $\times$  9.64'. Following the similar procedure in the AKARI FITS image the major and minor axes were found to be 6.58' and 3.05' and thus angular dimension was 6.58'  $\times$  3.05'. Similarly in the WISE FITS image, the major and minor axes were found to be 3.62' and 1.79' and thus angular dimension was 3.62'  $\times$  1.79'. The angular dimension was converted to linear dimension by using the formula,

$$l = d \times \theta \quad (5.1)$$

where angular dimension  $\theta$  should be converted to degrees. The distance(d) was estimated from Gaia data to be 979.49 pc. Thus the linear dimension of the region of interest was approximated to be 5.42 pc  $\times$  2.75 pc, 1.87 pc  $\times$  0.87 PC, and 1.03 pc  $\times$  0.51 pc in IRIS, AKARI, and WISE respectively.

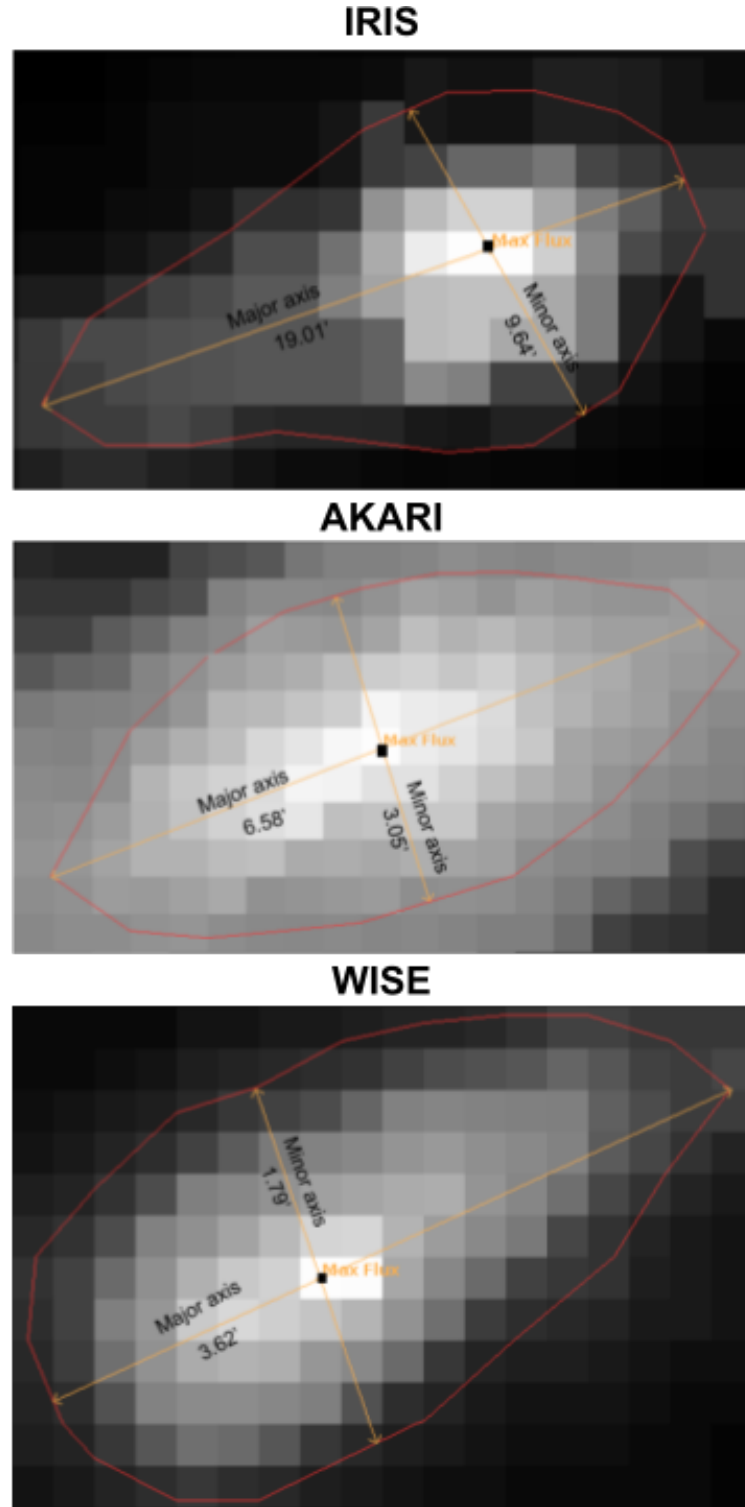


Figure 5.1: Region of Interest in IRIS, AKARI, and WISE FITS Images

The difference in dimensions of the isolated structure in different surveys is due to non-identical FITS image resolutions. The resolution of IRIS FITS image is the highest and that of WISE is the lowest. The direct proportionality between image resolution and structure thus resulted in the

greatest dimension for IRIS image and the lowest for WISE image.

Table 5.1: Dimensions of Dust Structure in Different Surveys

<b>Surveys</b>	<b>Angular Dimension</b>	<b>Linear Dimension</b>
IRIS (100 $\mu$ m)	19.01' $\times$ 9.64'	5.42 pc $\times$ 2.75 pc
AKARI (140 $\mu$ m)	6.58' $\times$ 3.05'	1.87 pc $\times$ 0.87 pc
WISE (22 $\mu$ m)	3.62' $\times$ 1.79'	1.03 pc $\times$ 0.51 pc

## 5.2 Flux Density Distribution

The flux density distribution was visualized in IRIS, AKARI, and WISE data using contour plots. These relative flux densities were later used for the calculation of dust color temperature.

Table 5.2: Flux Densities for Different Wavelengths

<b>Wavelength (<math>\mu</math>m)</b>	<b>Flux density (MJy sr<math>^{-1}</math>)</b>		
	<b>Minimum</b>	<b>Maximum</b>	<b>Average</b>
12	440.62	705.20	435.51
22	128.22	166.33	128.54
60	0.738	34.66	1.79
90	12.31	172.22	11.27
100	2.39	47.44	4.05
140	22.04	129.94	16.29

On plotting the maximum, minimum, and average flux densities each separately against their respective wavelengths, the scatter plot obtained was similar. This shows the uniform flux distribution across the surveys.

The data from Table 5.2 shows for a specific survey, there is a gradual increase in the relative flux densities with an increase in the wavelengths for longer wavelengths while for shorter wavelengths there is an inverse relation between flux density and wavelength. Moreover, from Figure 5.3 it can be seen that inner isocontours have higher relative flux densities than outer ones. This signifies the increasing density of the dust structure towards the center, which is in correspondence with the fact that the structure is a nebular region rather than a cavity region.

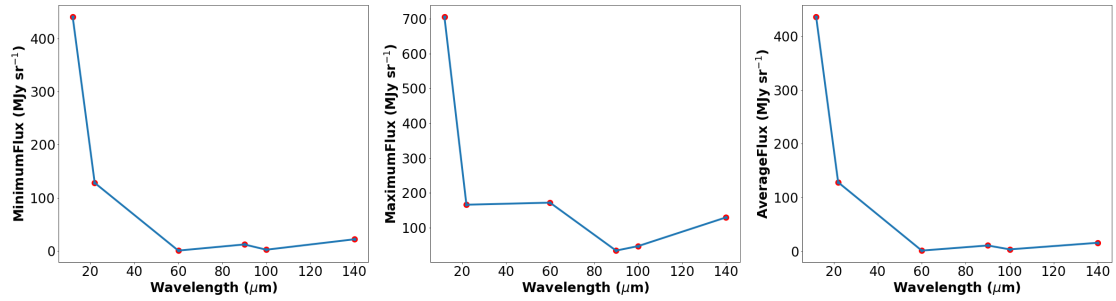


Figure 5.2: Scatter Plot of Flux Densities against Wavelengths

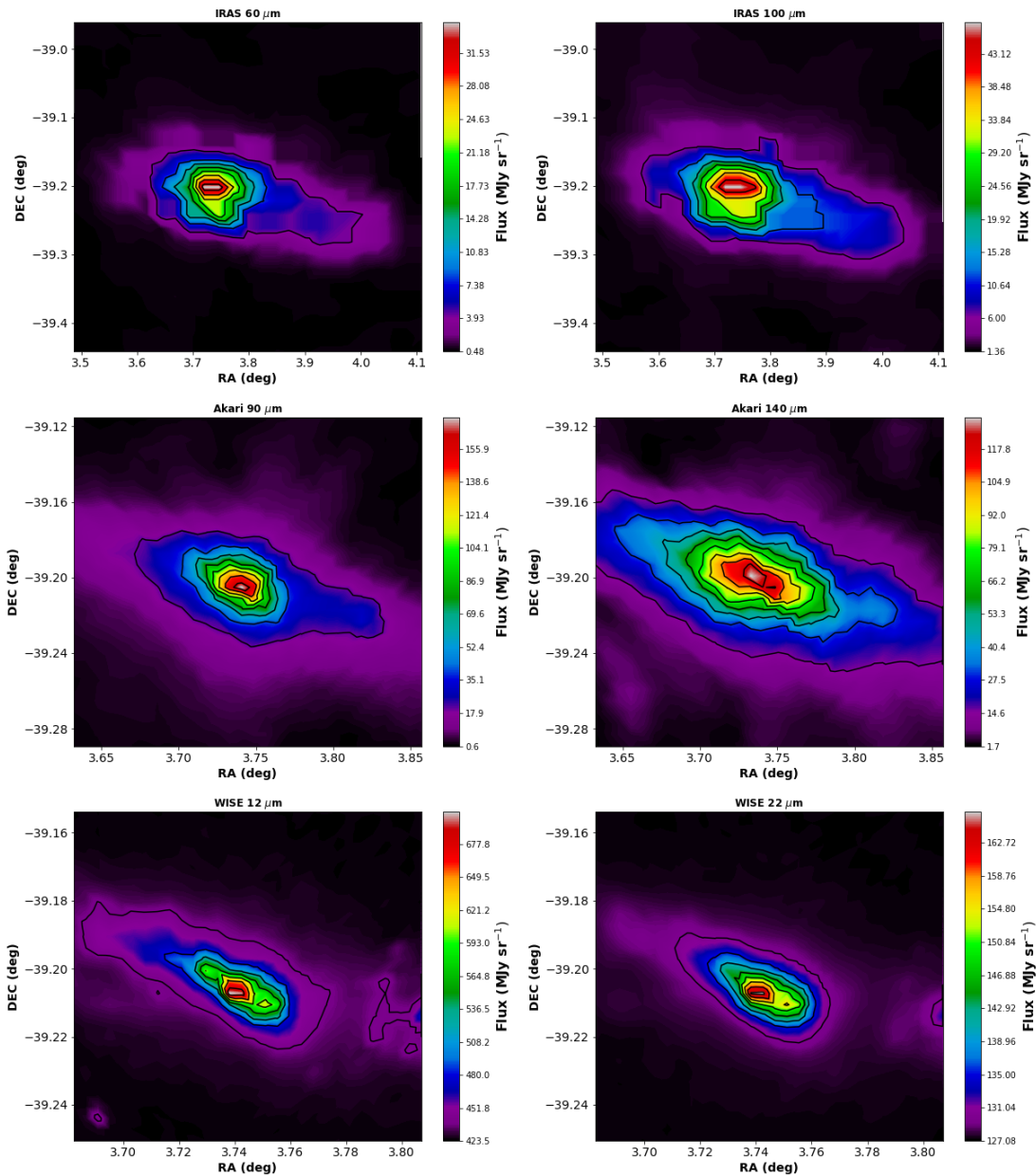


Figure 5.3: Contour Plots Showing Flux Density Distributions for Different Wavelengths

## 5.3 Flux Density Relation

Flux density at two different wavelengths for each survey was plotted against each other to determine the relationship between them. In IRIS data, the relationship between relative flux densities at 60 and 100  $\mu\text{m}$  was found to be linear with a correlation coefficient of 0.94. In AKARI data, the relationship between relative flux densities at 90 and 140  $\mu\text{m}$  was found to be parabolic with a correlation coefficient of 0.82. Similarly in WISE data, the relation between relative flux densities at 12 and 22  $\mu\text{m}$  was obtained to be linear with a correlation coefficient of 0.95.

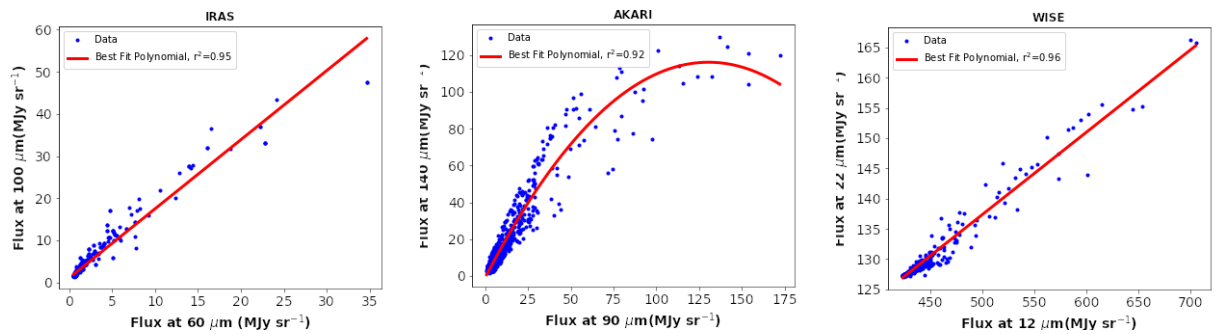


Figure 5.4: Flux density Relationship Between Different Wavelengths of the Same Survey

In general, the correlation between relative flux densities at two different wavelengths of the same survey is very high and positive which is as expected.

Table 5.3: Flux density Relation Between Different Wavelengths of the Same Survey

Surveys	Relation	Equation	Correlation Coefficient
IRIS	Linear	$F(100) = 0.58 \times F(60) - 0.55$	0.94
AKARI	Parabolic	-	0.82
WISE	Linear	$F(22) = 7.05 \times F(60) - 470.56$	0.95

## 5.4 Flux Density and Mass Relation

The relationship between flux density and mass of the structure was visualized using a contour plot for all the surveys. From side by side comparison, a direct relation between flux density and mass was observed. In all surveys, the regions with high flux density were also the denser regions. As the structure is nebular, the region with high flux density implies the accumulation of a larger amount

of dust in the region which makes it denser. The relationship visualized from the contour plot is in agreement with the explanation. However, in AKARI data, there was also observed lesser mass distribution in some regions with high flux density, and in WISE data, regions with low flux were observed to be comparatively denser. This might be due to the very low operating wavelength of WISE along with the presence of a lot of background sources nearby the structure.

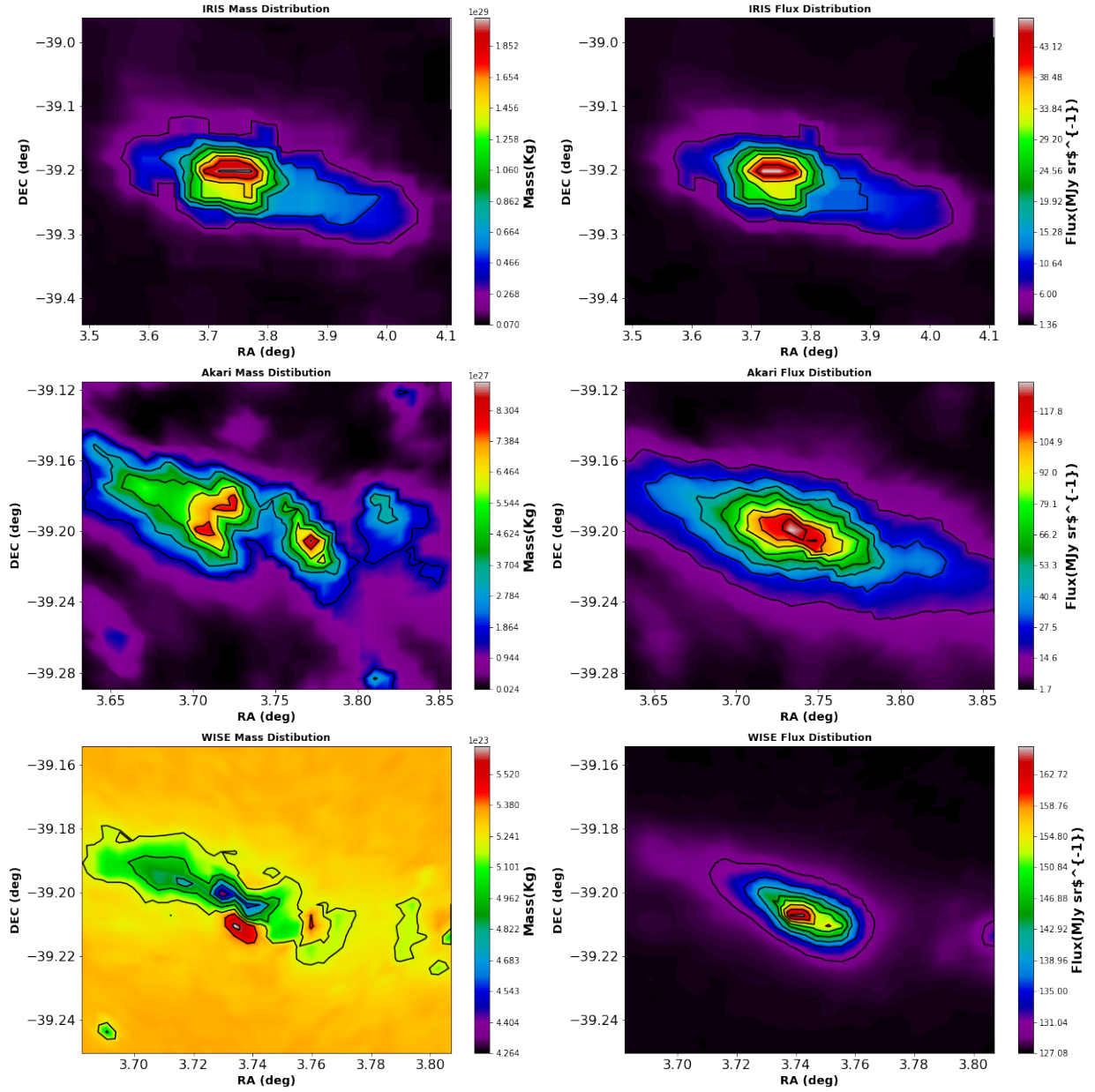


Figure 5.5: Contour Plots Showing Relationship Between Mass and Flux Distributions

## 5.5 Dust Color Temperature

The dust color temperature for IRIS, AKARI, and WISE data was calculated as given by equations 3.4, 3.7, and 3.10 respectively. The value of spectral emissivity,  $\beta$ , was chosen 2 assuming the dust components to be crystalline dielectrics. With the IRIS data, the temperature of the region of interest was found between a minimum value  $22.59 \pm 2.32$  K to maximum value  $36.82 \pm 4.30$  K with an offset of 14.23 K and an average temperature of  $28.22 \pm 0.18$  K. Using AKARI data, the temperature was found between a minimum of  $16.31 \pm 1.47$  K and a maximum of  $26.37 \pm 3.56$  K with an offset of 10.06 K and an average temperature of  $19.25 \pm 0.15$  K. Similarly in WISE data, the temperature was found between a minimum of  $307.24 \pm 4.69$  K and a maximum of  $353.72 \pm 18.54$  K with an offset of 46.48 K and an average temperature of  $316.62 \pm 0.81$  K.

Table 5.4: Temperature Distribution for Different Wavelengths

Surveys	Temperature (K)			
	Minimum	Maximum	Offset	Average
IRIS	$22.59 \pm 2.32$	$36.82 \pm 4.30$	14.23	$28.22 \pm 0.18$
AKARI	$16.31 \pm 1.47$	$26.37 \pm 3.56$	10.06	$19.25 \pm 0.15$
WISE	$307.24 \pm 4.69$	$353.72 \pm 18.54$	46.48	$316.62 \pm 0.81$

Since the temperature of the dust structure is low (around 15K) in IRIS and AKARI data, the structure under study is mostly composed of cool dust grains(Xilouris et al., 2012). Furthermore, the high value of offset temperature suggests that the structure might be evolving with disruptions from background radiative sources.

According to Wien's displacement law (for lower wavelengths and temperatures), the wavelength of black-body radiation ( $\lambda$ ) is inversely proportional to the temperature (T), given by

$$\lambda = \frac{b}{T} \quad (5.2)$$

where b is the Wien's displacement constant  $\approx 2898 \mu\text{mK}$ .

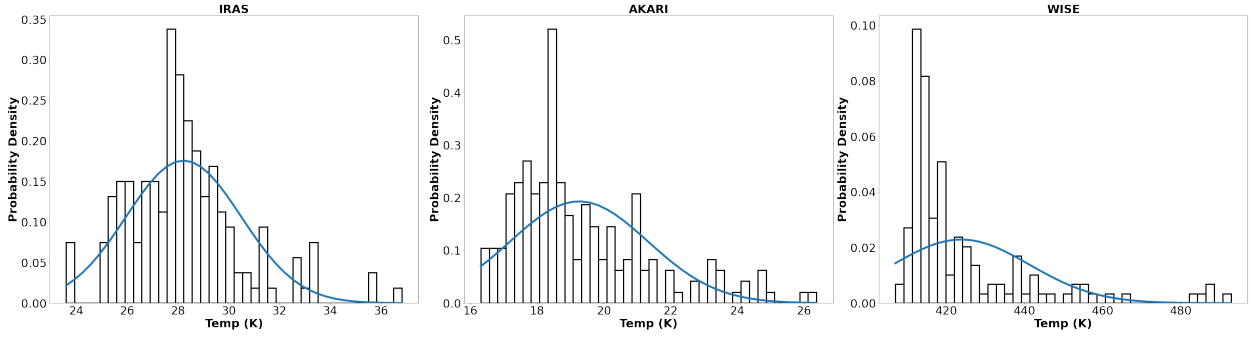


Figure 5.6: Gaussian Temperature Distributions in Different Surveys

From Table 5.4 it is seen that the temperature data for all surveys are in correspondence with Wien's displacement law. Moreover, the distribution of the temperature in all the surveys was found to be approximately Gaussian in nature as shown in Figure 5.6. Low temperatures and approximately Gaussian distributions of temperature suggest that the structure is tending towards thermodynamic equilibrium.

## 5.6 Dust Mass

The mass of the region of interest was calculated as given by equation 3.18 assuming the weighted grain size  $0.1 \mu\text{m}$ , grain density  $3000 \text{ kg.m}^{-3}$ , and grain emissivity 0.001 for  $100 \mu\text{m}$ . The distance calculated from the parallax method was also used for mass estimation. The estimated mass of the region of interest in IRIS, AKARI and WISE surveys were  $5.15 \times 10^{28} \text{ kg}$  ( $0.03 M_{\odot}$ ),  $3.14 \times 10^{27} \text{ kg}$  ( $1.6 \times 10^{-3} M_{\odot}$ ) and  $9.57 \times 10^{23} \text{ kg}$  ( $4.78 \times 10^{-7} M_{\odot}$ ) respectively.

Considering the general belief the mass of the gas in ISM is about 200 times greater than the mass of the dust (Hildebrand, 1983), mass of the gas in the structure was estimated to be  $1.03 \times 10^{31} \text{ kg}$  ( $5.15 M_{\odot}$ ),  $6.28 \times 10^{29} \text{ kg}$  ( $0.31 M_{\odot}$ ) and  $1.91 \times 10^{26} \text{ kg}$  ( $9.75 \times 10^{-5} M_{\odot}$ ) in IRIS, AKARI and WISE surveys respectively.

From the study of contour plots between temperature and mass for different surveys, it was found that there exists no direct correspondence between temperature and mass distribution in IRIS and AKARI data. However, in WISE data, the region with a high-temperature distribution was found to have a higher mass distribution, and those with a low-temperature distribution were found to have a low mass distribution as shown in Figure 5.8.

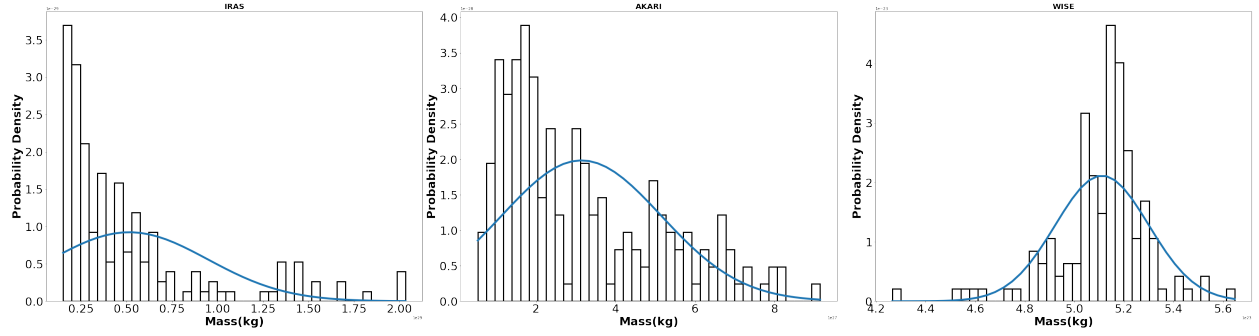


Figure 5.7: Gaussian Mass Distributions in Different Surveys

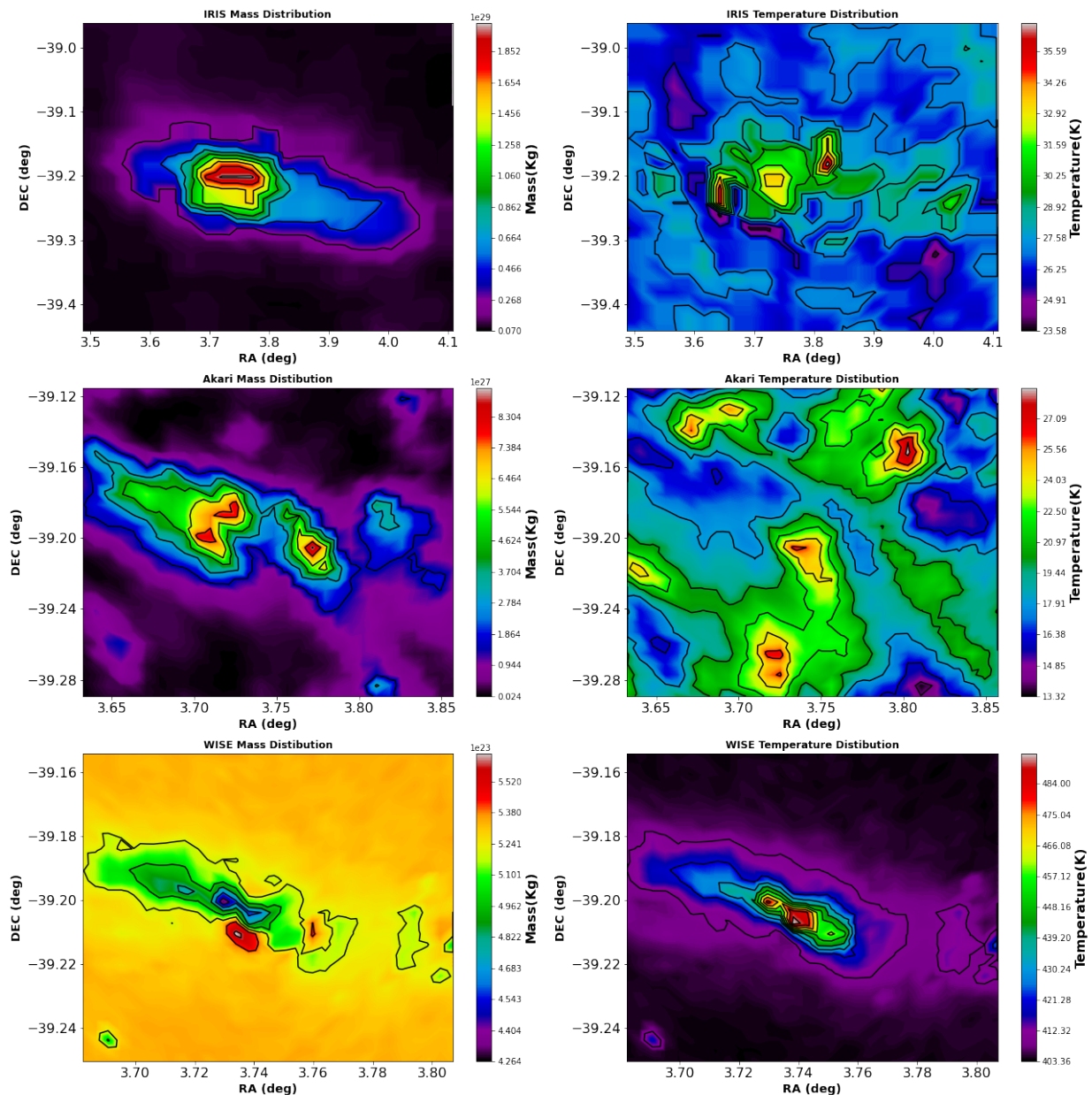


Figure 5.8: Mass and Temperature Contour Plots in Different Surveys

## 5.7 Jean's Mass

Jean's mass was estimated assuming dust structure as a non-degenerate mass. Average Jean's mass for IRIS, AKARI, and WISE data were estimated to be  $3.56 \times 10^{32}$  kg ( $178.44 M_{\odot}$ ),  $2.42 \times 10^{32}$  kg ( $121.47 M_{\odot}$ ) and  $3.98 \times 10^{33}$  kg ( $2001.93 M_{\odot}$ ) respectively. Since Jean's masses for all the surveys are far greater than the masses of the structure, theoretically the gravity of the structure is not dominant enough for gravitational collapse. Thus there seems no possibility of star formation within the region of interest.

Table 5.5: Mass of Dust, Gas and Jean's Mass for Different Surveys

Wavelength ( $\mu\text{m}$ )	Mass ( $M_{\odot}$ )		
	Mass of Dust	Mass of Gas	Jean's Mass of Dust
22 (WISE)	$10^{-7}$	$9.75 \times 10^{-5}$	2001.93
100 (IRIS)	0.03	5.15	178.44
140 (AKARI)	$1.6 \times 10^{-3}$	0.31	121.47

## 5.8 Inclination Angle

The estimated major axis (a) and minor axis (b) from Aladin v10.0 were used to calculate the inclination angle according to equation 3.30 assuming an average intrinsic flatness of the nebula to be 0.23. Thus estimated inclination angles were  $62.32^{\circ}$ ,  $65.57^{\circ}$  and  $62.27^{\circ}$  respectively in IRIS, AKARI and WISE data. The inclination angles are approximately the same for all the surveys which is as expected because it represents the inclination of the structure from the galactic plane which should be equivalent in all the surveys. The inclination angle is neither close to zero (face-on) nor close to  $90^{\circ}$  (edge-on) (Jha & Aryal, 2018b). Face-on implies a spherical structure and edge-on implies an ellipsoidal structure. Moreover, the ratio of the minor axis to the major axis is 0.51, 0.46, and 0.49 in IRIS, AKARI, and WISE data. This implies the dust structure is neither spherical nor ellipsoidal, however, somewhat deviated towards an ellipsoidal structure.

Table 5.6: Inclination Angle of the Dust Structure in Different Surveys

Surveys	Inclination Angle (degrees)	b/a Ratio
IRIS (100 $\mu$ m)	62.32	0.51
AKARI (140 $\mu$ m)	65.57	0.46
WISE (22 $\mu$ m)	62.27	0.49

## 5.9 Spectral Emissivity

Spectral emissivity was plotted for all the survey data against their respective average temperature. In IRIS and AKARI data, the relationship between spectral emissivity/index and average temperature is parabolic with a correlation coefficient = 1. However, in WISE data, there exists a 7th-degree polynomial relation between spectral emissivity/index and average temperature as shown in Figure 5.9.

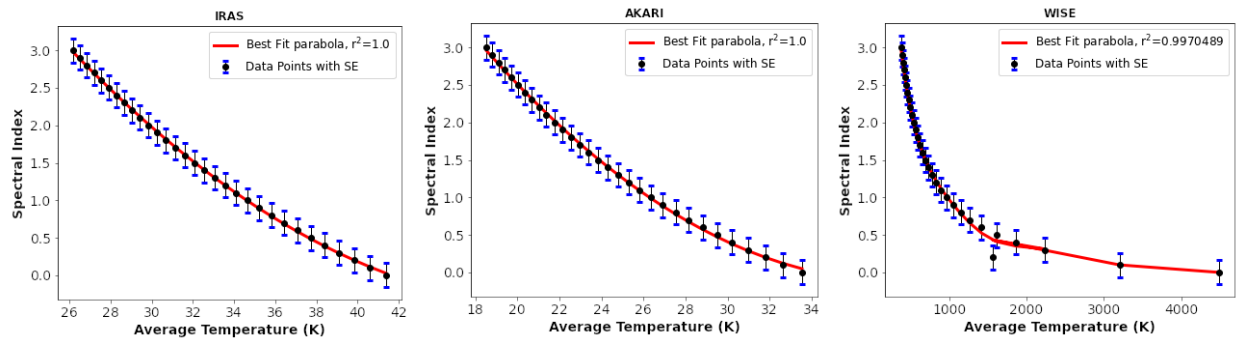


Figure 5.9: Emissivity and Average Temperature Relation for All Surveys

## 5.10 Visual Extinction

Visual extinction was estimated for long wavelengths of IRIS and AKARI data. The average visual extinction for IRIS 100  $\mu$ m and AKARI 140  $\mu$ m data were  $3.32 \times 10^{-12}$  and  $2.02 \times 10^{-13}$ . The relation between visual extinction and temperature was plotted for IRIS and AKARI data. In IRIS data the relationship was more or less linear with a correlation coefficient of 0.18 while in AKARI data the relationship was found to be non-linear, somehow inverse parabolic with a correlation coefficient of 0.41 as shown in Figure 5.10.

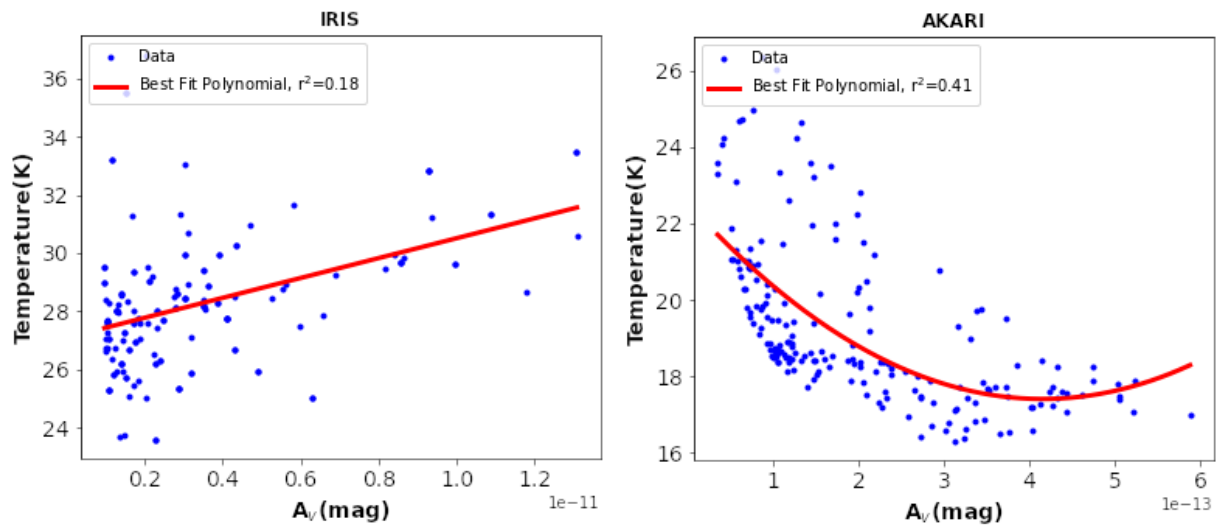


Figure 5.10: Plot of Visual Extinction Against Temperature in IRIS and AKARI Data

## 5.11 Background Sources

Background astronomical objects around the dust structure were obtained from the SIMBAD astronomical database. Within the radius of  $20'$  around the coordinates RA(ICRS):  $3.79^\circ$  and Dec.(ICRS):  $-39.20^\circ$ , there were 809 astronomical objects. Among them the number of stars is dominant. The types of astronomical objects along with their numbers are shown in Table 5.7.

Table 5.7: Background Sources Obtained From SIMBAD

Sources	Counts
Star	225
Cepheid	143
Galaxy	89
Active Galactic Nucleus (AGN)	81
Globular Cluster (GlCl)	50
X-ray Source	42
High Mass X-ray Binary (HMXB)	26
Emission Object (EmObj)	22
Low Mass X-ray Binary (LMXB)	20
Planetary Nebula (PN)	20
HII 21cm	12
Emission Line Galaxy (EmG)	9
Candidate WD	2

The presence of such a large number of astronomical objects around the structure has a major influence on the properties of the structure. The approximate normal temperature distribution of the structure can be interpreted as the influence of these background astronomical objects. From the analysis of Figure 5.11 it was found that in the regions of higher mass, astronomical objects like stars, cepheids, and emission objects are dominant. Since stars are continually radiating energy, cepheids are radially pulsating causing variation in their diameter and temperature, and emission objects as the name suggests emit energy, the distribution of mass and temperature is highly influenced by their presence in the background.

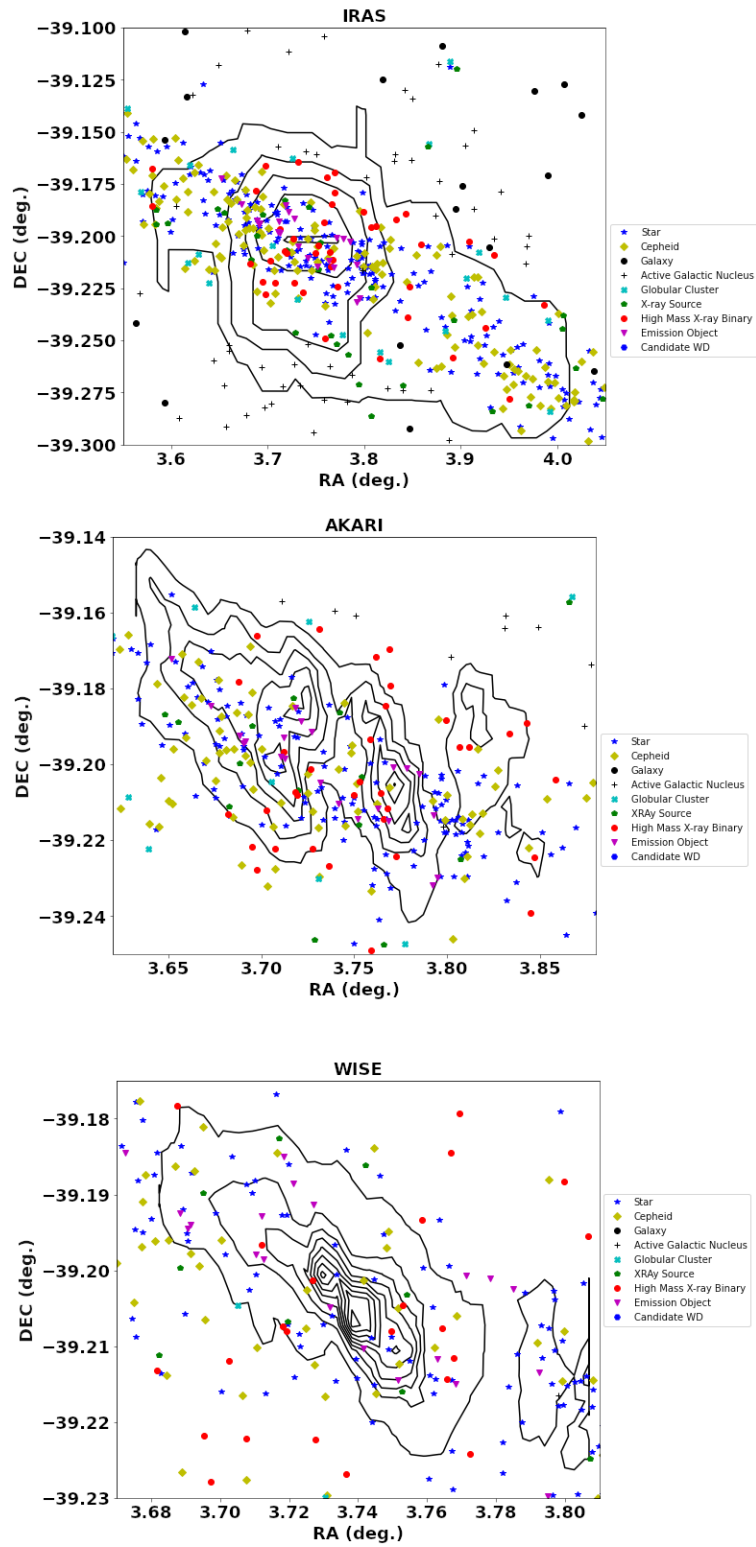


Figure 5.11: Background Objects and Mass Distribution in Different Surveys

# Chapter 6

## CONCLUSION AND FUTURE ENHANCEMENTS

### 6.1 Conclusion

Various properties such as infrared flux density distribution and relation, dust color temperature, dust mass, Jean's mass, distance, inclination angle, spectral emissivity, and visual extinction of the dust structure near the white dwarf WD0011-399 located at RA(J2000): 00 13 47.48, Dec.(J2000): -39 37 24.28 were studied. The following are the major conclusions of the project work:

- The size of the dust structure is estimated to be  $19.01' \times 9.64'$  ( $5.42 \text{ pc} \times 2.75 \text{ pc}$ ),  $6.58' \times 3.05'$  ( $1.87 \text{ pc} \times 0.87 \text{ pc}$ ) and  $3.62' \times 1.79'$  ( $1.03 \text{ pc} \times 0.51 \text{ pc}$ ) in IRIS, AKARI and WISE surveys respectively.
- For the same survey the relative flux density is directly proportional to the wavelength in case of longer wavelengths i.e.  $60\text{-}140 \mu\text{m}$ . However, the relation is just the opposite in the case of shorter wavelength i.e.  $12\text{-}22 \mu\text{m}$ .
- The average temperature of the isolated region is estimated to be  $28.22 \pm 0.18 \text{ K}$  in IRIS,  $19.25 \pm 0.15 \text{ K}$  in AKARI, and  $316.62 \pm 0.81 \text{ K}$  in WISE data. The relation between wavelength and temperature is in accordance with Wien's displacement law.
- The study of the contour map shows there is no direct relation between the distribution of mass and temperature in IRIS and AKARI data. However, there exists a direct relation between them in WISE data.
- There exists a linear relation between the distribution of temperature and visual extinction in IRIS and non-linear (parabolic) in AKARI data.
- The central part of the isolated region is hotter as well as denser than the outer region representing the central region is thermally active and dense while the outer region is thermally stable.

- The distance of the dust structure is estimated to be 979.49 pc.
- The study of background sources in the SIMBAD database shows a large number of background objects near the structure which might be responsible for the contribution of dust temperature and dust mass within the dust structure.
- The Temperature and Mass distribution is close to the Gaussian distribution which might indicate asymmetric distribution of ISM sources, such as; dense core, part of cloud, radio (sub-mm) source, etc., which are observed in the SIMBAD database.
- Inclination angle was found to be  $62.32^\circ$ ,  $65.57^\circ$  and  $62.27^\circ$  with minor to major axis ratios of 0.51, 0.46, and 0.49 in IRIS, AKARI, and WISE data respectively. This shows that the isolated region within the dust structure is neither face-on nor edge-on, however, slightly deviated from spherical shape.

## 6.2 Future Enhancements

The project work has a wide scope for enhancements in the future. Some of them are described as follows:

- Multiwavelength band properties of the structure are not studied in this project work which can be studied in the future. It gives a better idea about the composition of the structure. It can also reveal the role of highly energetic radiation in the shaping process.
- Discrete sources can be located using SIMBAD and analyzed in detail by projecting onto the contour maps of various wavelengths.
- The flow of dust was not studied in this work which can be studied as well as visualized with hydrodynamics simulations.

# Bibliography

- Bertout, C., Smolders, K., Acke, B., Verhoelst, T., Blommaert, J., Decin, L., ... others (2010). Special feature on akari results e1. *Astronomy & Astrophysics*, 514.
- Böhm-Vitense, E. (1992). *Introduction to stellar astrophysics: Volume 3* (Vol. 3). Cambridge University Press.
- Boulanger, F., Cox, P., & Jones, A. (2000). Dust in the interstellar medium. In *Astronomie spatiale infrarouge, aujourd’hui et demain infrared space astronomy, today and tomorrow* (pp. 251–335). Springer.
- Brown, A. G., Vallenari, A., Prusti, T., De Bruijne, J., Babusiaux, C., Biermann, M., ... others (2021). Gaia early data release 3-summary of the contents and survey properties. *Astronomy & Astrophysics*, 649.
- C. A. Beichman, H. J. H. P. E. C., G. Neugebauer, & Cheste, T. J. (1988). *Infrared astronomical satellite (iras) catalogs and atlases* (Vol. 1) (No. **NAS 1.61:1190-VOL-1**).
- Carroll, B., & Ostlie, D. (2014). *An introduction to modern astrophysics* (2nd ed.). Pearson Education Limited.
- Cosmos, C. (2018). *Herschel discovers infrared light*.
- Dufour, P., Blouin, S., Coutu, S., Fortin-Archambault, M., Thibeault, C., Bergeron, P., & Fontaine, G. (2016). The montreal white dwarf database: a tool for the community. *arXiv preprint arXiv:1610.00986*.
- Dupac, X., Bernard, J.-P., Boudet, N., Giard, M., Lamarre, J.-M., Mény, C., ... others (2003). Inverse temperature dependence of the dust submillimeter spectral index. *Astronomy & Astrophysics*, 404(1), L11–L15.
- Ferriere, K. M. (2001). The interstellar environment of our galaxy. *Reviews of Modern Physics*, 73(4), 1031.
- Gautam, A., & Chhatkuli, D. (2020). Planck function distribution in the far infrared cavity nearby agb star at galactic latitude 0.6 °. *Journal of Nepal Physical Society*, 6(2), 97–103.
- Haynes, M. P., & Giovanelli, R. (1984). Neutral hydrogen in isolated galaxies. iv-results for the arecibo sample. *The Astronomical Journal*, 89, 758–800.
- Herwig, F. (2005). Evolution of asymptotic giant branch stars. *Annu. Rev. Astron. Astro-*

*phys.*, 43, 435–479.

Hildebrand, R. H. (1983). The determination of cloud masses and dust characteristics from submillimetre thermal emission. *Quarterly Journal of the Royal Astronomical Society*, 24, 267.

Holmberg, E. (1946). Investigations of the systematic errors in the apparent diameters of the nebulae. , 117.

Jha, A., & Aryal, B. (2018a). Dust color temperature distribution of two fir cavities at iris and akari maps. *Journal of Astrophysics and Astronomy*, 39(2), 1–7.

Jha, A., & Aryal, B. (2018b). Dust color temperature distribution of two fir cavities at iris and akari maps. *Journal of Astrophysics and Astronomy*, 39(2), 5–6.

Karttunen, H., Kröger, P., Oja, H., Poutanen, M., & Donner, K. J. (2007). *Fundamental astronomy* (Vol. 4). Springer.

Kundt, W. (2004). *Astrophysics: a new approach*. Springer Science & Business Media.

Maoz, D. (2016). *Astrophysics in a nutshell* (Vol. 16). Princeton university press.

McCook, G. P., & Sion, E. M. (1999). A catalog of spectroscopically identified white dwarfs. *The Astrophysical Journal Supplement Series*, 121(1), 1.

Mcglynn, K., T.and Scollick, & White, N. (1997). Skyview: The multi-wavelength sky on the interne. *New Horizons from Multi-Wavelength Sky Surveys*. doi: 10.1007/978-94-009-1485-8\_17

Miville-Deschénes, M.-A., & Lagache, G. (2005). Iris: a new generation of iras maps. *The Astrophysical Journal Supplement Series*, 157(2), 302.

Osterbrock, D. E. (2000). A fortunate life in astronomy. *Annual Review of Astronomy and Astrophysics*, 38(1), 1–33.

Paudel, M., Bhandari, P., & Bhattacharai, S. (2021). Study of dust cavity around the white dwarf wd 0352-049 in infrared astronomical satellite map. *Journal of Nepal Physical Society*, 7(2), 110–118.

Paudel, M., & Bhattacharai, S. (2021). Studies of the properties of dust structure nearby the supernova remnants g053. 41+ 00.3, g053. 9+ 00.2 and g053. 1+ 00.3 using data from iris and akari. *Journal of Nepal Physical Society*, 7(3), 59–66.

Paudel, M. S. (2013). A new isolated far infrared nebula at- 37° galactic latitude in iras map.

Paudel, M. S. (2018). Study of dust colour temperature and mass profile of two new far

infrared nebular structure in infrared astronomical satellite map.

Schmadel, L. (2003). *Dictionary of minor planet names*. Springer Science Business Media.

doi: 10.1007/978-3-540-29925-7\_3725

Schnee, S. L., Ridge, N. A., Goodman, A. A., & Li, J. G. (2005). A complete look at the use of iras emission maps to estimate extinction and dust temperature. *The Astrophysical Journal*, 634(1), 442.

Thapa, A., Paudel, M., & Pant, B. (2019). An infrared survey of isolated nebular structures at galactic latitudes 16.98 & 1.98 in aras map. *Journal of Nepal Physical Society*, 5(1), 74–84.

Tielens, A. G. (2005). *The physics and chemistry of the interstellar medium*. Cambridge University Press.

Wenger, M., Ochsenbein, F., Egret, D., Dubois, P., Bonnarel, F., Borde, S., ... others (2000). The simbad astronomical database-the cds reference database for astronomical objects. *Astronomy and Astrophysics Supplement Series*, 143(1).

Wood, D. O., Daugherty, D. A., & Myers, P. C. (1994). Iras images of nearby dark clouds. *Astrophysics Journal and Supplement Series*, 95, 457–501.

Wright, E. L., Eisenhardt, P. R., Mainzer, A. K., Ressler, M. E., Cutri, R. M., Jarrett, T., ... others (2010). The wide-field infrared survey explorer (wise): mission description and initial on-orbit performance. *The Astronomical Journal*, 140(6).

Xilouris, E., Tabatabaei, F., Boquien, M., Kramer, C., Buchbender, C., Bertoldi, F., ... others (2012). Cool and warm dust emission from m 33 (herm33es). *Astronomy & Astrophysics*, 543, A74.

Young, K., Phillips, T., & Knapp, G. (1993). Circumstellar shells resolved in iras survey data. ii-analysis. *The Astrophysical Journal*, 409, 725–738.